



HAL
open science

Towards stratigraphic-thermo-mechanical numerical modelling: Integrated analysis of asymmetric extensional basins

Attila Balázs, Liviu Matenco, Didier Granjeon, Katharina Alms, Thomas Francois, Orsolya Sztanó

► To cite this version:

Attila Balázs, Liviu Matenco, Didier Granjeon, Katharina Alms, Thomas Francois, et al.. Towards stratigraphic-thermo-mechanical numerical modelling: Integrated analysis of asymmetric extensional basins. *Global and Planetary Change*, 2021, 196, pp.103386. 10.1016/j.gloplacha.2020.103386 . insu-03097842

HAL Id: insu-03097842

<https://insu.hal.science/insu-03097842>

Submitted on 5 Jan 2021

HAL is a multi-disciplinary open access archive for the deposit and dissemination of scientific research documents, whether they are published or not. The documents may come from teaching and research institutions in France or abroad, or from public or private research centers.

L'archive ouverte pluridisciplinaire **HAL**, est destinée au dépôt et à la diffusion de documents scientifiques de niveau recherche, publiés ou non, émanant des établissements d'enseignement et de recherche français ou étrangers, des laboratoires publics ou privés.



Distributed under a Creative Commons Attribution - NonCommercial - NoDerivatives 4.0 International License



Research Article

Towards stratigraphic-thermo-mechanical numerical modelling: Integrated analysis of asymmetric extensional basins

Attila Balázs^{a,*}, Liviu Mațenco^b, Didier Granjeon^c, Katharina Alms^d, Thomas François^e, Orsolya Sztanó^f^a ETH Zürich, Geophysical Fluid Dynamics Group, Institute of Geophysics, Zürich, Switzerland^b Department of Earth Sciences, Faculty of Geosciences, Utrecht University, Utrecht, the Netherlands^c Geosciences Division, IFPEN, IFP Energies Nouvelles, Rueil-Malmaison, France^d Fraunhofer IEG, Institution for Energy Infrastructures and Geothermal Systems IEG, Bochum Location, Lennerhofstrasse 140, 44801 Bochum, Germany^e Université Paris-Saclay, CNRS, GEOPS, Orsay 91405, France^f Eötvös Loránd University, Department of Geology, Budapest, Hungary

ARTICLE INFO

Keywords:

Asymmetric extension
Sedimentation
Heat flow evolution
Subsidence history
Depositional systems
Pannonian Basin

ABSTRACT

Subsidence and uplift patterns and thermal history of sedimentary basins are controlled by tectonics, mantle dynamics and surface processes, such as erosion, sediment transport and deposition and their links to climatic variations. We use combined thermo-mechanical and stratigraphic numerical modelling techniques to quantify the links between tectonic and surface processes. We aim to assess the thermal evolution and subsidence rates of asymmetric extensional basins during the syn- and post-rift times by simulating different erosion and sedimentation rates. We analyse the 3D sedimentary architecture and facies distribution of the depocenters. Model results are validated by observations in the Pannonian Basin of Central Europe. Extensional reactivation of inherited suture zones creates asymmetric basin systems controlled by large-scale detachments or low-angle normal faults, where crustal and lithospheric mantle thinning are often rheologically decoupled. Subsidence rates and basement heat flow in the depocenters show large variabilities during asymmetric extension and post-rift evolution controlled by their initial position from the suture zone and migration of deformation. Transient heat flow anomalies mirror crustal exhumation of footwalls, sediment blanketing and erosion effects in the basins. Enhanced erosion and sedimentation facilitate lower crustal deformation and elastic flexure of the weak, extended lithosphere leading to accentuated differential uplift and subsidence during the syn- and post-rift basin evolution. Tectonics, climate and autogenic processes control transgressive-regressive cycles at different time-scales together with the overall sedimentary facies distribution. In our models assuming wet climate the high subsidence rate often outpaces moments of eustatic water-level fall preventing relative base-level fall and enhances the effects of autogenic processes, such as lobe switching processes.

1. Introduction

The inherent links between tectonics, mantle dynamics and surface processes such as erosion and sedimentation coupled to climatic variations, have been long recognized as the main drivers for the evolution of orogens (e.g., Whipple, 2009; Erdos et al., 2014; Ueda et al., 2015) and sedimentary basin systems (e.g., Burov and Poliakov, 2003; Bialas and Buck, 2009; Olive et al., 2014; Hart et al., 2017; Ballato et al., 2019). Understanding the complex interplay between tectonic and surface processes requires the joint application of thermo-mechanical and

stratigraphic modelling techniques (e.g., Wu et al., 2018; Andrés-Martínez et al., 2019; Theunissen and Huisman, 2019). Simulations of erosion, sediment transport and deposition together with modelling of the basin evolution are amongst the most challenging objectives, because tectonic and sedimentary processes, such as floods or sediment gravity flows act on a wide range of spatial and temporal scales (e.g., Armitage et al., 2011; Postma et al., 2014). Furthermore, quantitative understanding of the thermal evolution and burial history of the sedimentary basins help for the assessment of geo-resources, such as geothermal energy, hydrocarbons or freshwater. Basement heat flow

* Corresponding author at: ETH Zurich, Geophysical Fluid Dynamics Group, Institute of Geophysics, Sonneggstrasse 5, CH8092 Zürich, Switzerland.
E-mail address: attila.balazs@erdw.ethz.ch (A. Balázs).

evolution is one of the prime parameters for basin analysis (Theissen and Rüpke, 2010). Its quantification is challenging due to its links and feedbacks between tectonics, surface processes and climate (Ter Voorde and Bertotti, 1994), and therefore its modelling requires an integrated approach.

The spatial and temporal variation of differential vertical movements and the associated evolution of sedimentary environments in extensional sedimentary basins are primarily controlled by the relationship between crustal and lithospheric thinning, influenced by the rheological layering and by the evolution of the underlying asthenosphere (Burov and Yamato, 2008; Dressel et al., 2017; Naliboff et al., 2017). Owing to inherited orogenic cycles, extension generally affects a heterogeneous continental lithosphere (Duretz et al., 2016). These heterogeneities, such as nappe contacts or former suture zones are considered rheological weak zones and localizes deformation (Heron et al., 2016; Petersen and Schiffer, 2016) controlling the evolution of asymmetric extensional basins (Balázs et al., 2017a).

The architecture of sedimentary basins is the result of the interplay between relative sea-level changes and sediment supply (Schlager, 1993) combined with sediment transport processes (e.g., Burgess et al., 2019). Relative water-level changes are controlled by eustatic sea-level variations and tectonics, their relative importance varies during basin evolution from extension to post-rift times (Martins-Neto and Catuaneanu, 2010; Balázs et al., 2018a; Matenco and Haq, 2020). In active extensional settings the migration of deformation and differential vertical movements play an important role in the 3D sedimentary architecture (Andrić et al., 2017; Balázs et al., 2017a; Hou et al., 2020), while during post-rift times eustatic variations often outpace the slower subsidence and together with autogenic processes they control sedimentary sequences (Csató et al., 2014; Harris et al., 2020). Separating and understanding the distinct basin-wide or global scale allogenic processes, such as environmental, climatic and tectonic forcing factors and the internally generated, local, short-term autogenic forcing in the sedimentary record is fundamental for pertinent basin analysis (e.g., Yang et al., 1998; Kim et al., 2013).

In this study, we aim to investigate the interactions between tectonics and surface processes in asymmetric extensional sedimentary basins by applying a joint method of thermo-mechanical and stratigraphic numerical modelling. In a series of experiments, we test the influence of erosion and sedimentation rates and different values of initial crustal and lithospheric thickness during extension and subsequent post-rift evolution. A wet and dry climatic scenario is computed by using different erosion and sedimentation rates in both the thermo-mechanical and stratigraphic models. We compare the heat flow and temperature evolution of the sedimentary basins under these conditions. The wet scenario simulates long-term climatic optimums, such as the Mid-Miocene Climatic Optimum (ca. 17–14 Ma) and the period of late Miocene increased precipitation and erosion inferred for the evolution in Central Europe (Böhme, 2003). This integrated approach yields quantitative understanding of the interplay between tectonics and surface processes, heat flow and burial history, lithological distribution and the formation of unconformities and their connection with different forcing factors.

2. Numerical methods

We combined lithospheric-scale numerical simulations of asymmetric extension by applying the thermo-mechanical code Flamar v12 (Burov and Yamato, 2008) and the basin-scale stratigraphic forward modelling code DionisosFlow (Granjeon, 2019). Our modelling approach enables the one-way joint run of Flamar and DionisosFlow (Fig. 1; Appendix A, B). The thermo-mechanical code is particularly well suited to study the dynamics of lithospheric extension and topographic evolution.

Depocenter geometries and total sediment loaded basement vertical motions were extracted from the thermo-mechanical model in 2D along

a 2D dip line (X,Y) at each timestep. In two subsequent 3D stratigraphic simulations, these calculated basement subsidence and uplift values were uniformly extended in the third, Z dimension (models M1wet, M1dry) in the absence of any along-strike variations (Fig. 1). In two further 3D stratigraphic experiments (M2wet, M2dry) we defined finite fault segments in the third (Z) dimension and thus imposed along-strike variations of the calculated subsidence values (Fig. 1b and Fig. B2 in Appendix B). In these two latter models we assumed an average fault displacement to fault length ratio of 1:30 (Childs et al., 2009). The hanging wall subsidence and footwall uplift values decrease towards the sides of the 3D stratigraphic model domain mirroring a relay zone and asymmetric footwall geometries (geometry II. in Fig. 1b). We choose this imposed segmented fault geometry and subsidence pattern to simulate the observed normal fault pattern of the Pannonian Basin (Horváth et al., 2015). The resulted basement subsidence history was then imported into the high-resolution stratigraphic simulations at each timestep where erosion, sediment transport (Fig. 2) and deposition and the overall basin-scale sedimentary architecture and 3D facies distribution were simulated at high resolution (i.e. meter-scale vertical resolution). Both Flamar and DionisosFlow models use a dynamic timestep scheme, DionisosFlow uses a finer temporal resolution (i.e. hundreds of years) and, therefore, linear interpolation was made between the time steps (thousands of years) of the thermo-mechanical modelling results. Further model description and model limitations are shown in the supplementary information file (Appendix A, B).

Despite the different numerical approach of the two software, the calculated syn- and post-rift sedimentary thicknesses are similar in the thermo-mechanical and in the subsequent stratigraphic numerical models. Nevertheless, the much finer temporal and vertical resolution of DionisosFlow enable a more detailed simulation and sedimentary interpretation for the stratigraphic architecture. Furthermore, DionisosFlow simulates multiple sediment classes and thus the sedimentary facies distribution can be analysed.

2.1. Thermo-mechanical numerical modelling method

Lithospheric-scale models were performed by the 2D thermo-mechanically coupled finite element code Flamar v12 (Burov and Yamato, 2008) based on the earlier Flac-Para(o)voz algorithm (Poliakov et al., 1993). In the Lagrangian method, incremental displacements are added to the grid coordinates allowing the mesh to move and deform with the material. This allows for the solution of large-strain problems while using locally the small-strain formulation. The code locally solves full Newtonian equations of motion in a continuum mechanics approximation in 2D. The equations are coupled with the heat transfer and further constitutive equations using temperature and pressure dependent densities and including linear elasticity, Mohr–Coulomb failure criterion for brittle deformation (faults) and pressure–temperature and strain-rate dependent viscous deformation (Burov and Yamato, 2008). Linear cohesion softening is used for effective localisation of plastic deformation (Huismans and Beaumont, 2003).

This method handles a free upper surface affected by simplified surface processes. Erosion and sedimentation were simulated by a linear diffusion law, where different diffusion coefficients (k_e) correspond to different erosion and sedimentation rates.

$$\frac{dh}{dt} = k_e \frac{\partial^2 h}{\partial x^2} \quad (1)$$

where h is topography, t is time, x is the horizontal dimension. Our modelling setup involves a 1000 km wide and 450 km deep 2D section. The horizontal grid resolution is 2 km and the vertical grid resolution varies from 1.2 to 3 km. The accuracy of the vertical displacement is in the order of 10 m. We applied a sum of 2 cm/yr constant divergence velocity condition at the sides of the model simulating the Pannonian Basin extension rate during its syn-rift phase. This velocity is set to zero

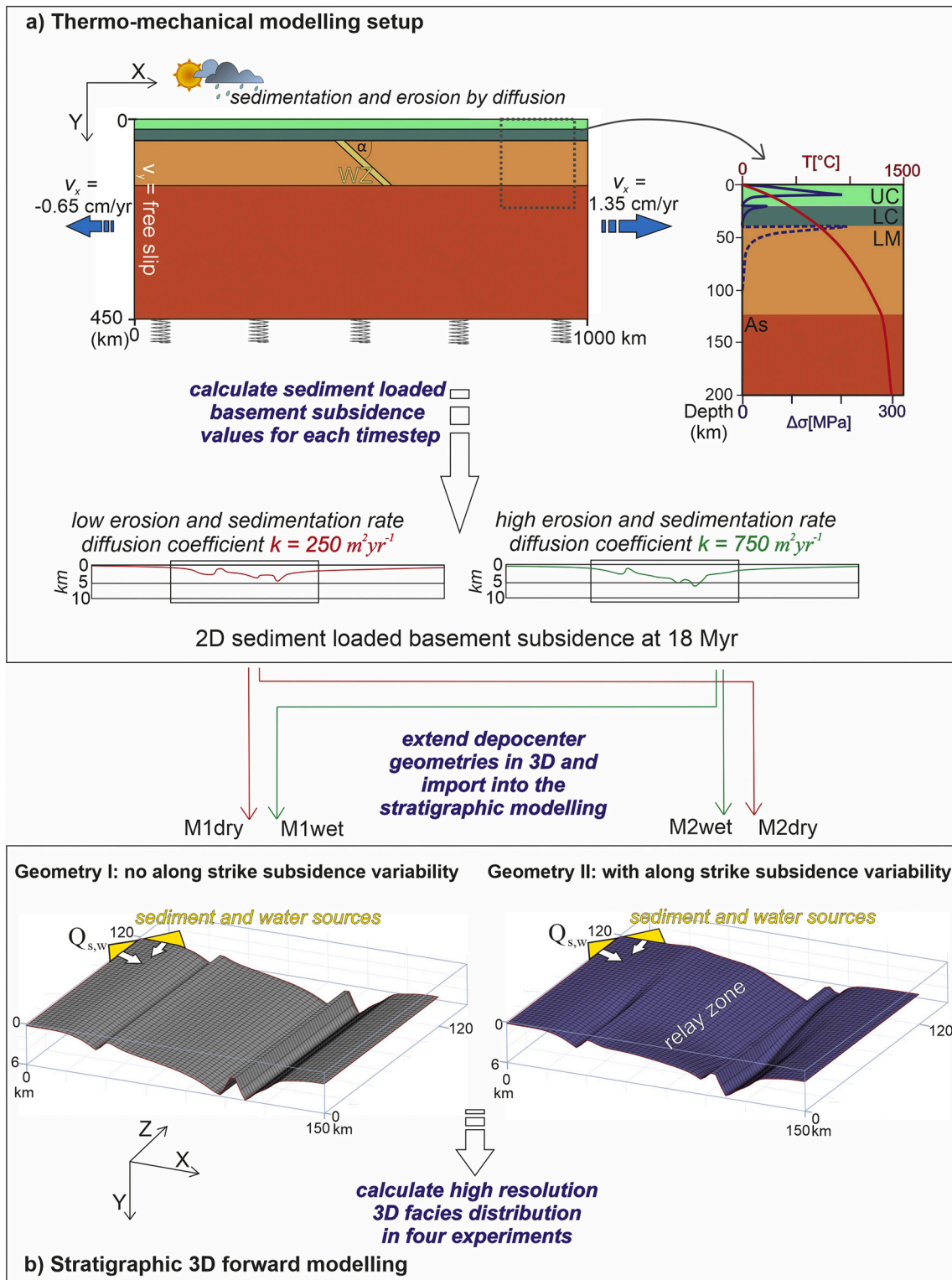


Fig. 1. Workflow of the thermo-mechanical and stratigraphic numerical models. The tectonic vertical movements imposed in the stratigraphic model were extracted from the thermo-mechanical models. (a) UC: upper crust, LC: lower crust, LM: lithospheric mantle, As: asthenosphere. Springs indicate lithostatic pressure (Winkler basement) applied at the base of the thermo-mechanical model. An initial tilted rheological weakness zone (WZ) is implemented in the lithosphere simulating a former suture zone. (b) Basement geometries in sediment transport and deposition forward modelling of three half-grabens with (right) and without (left) along-strike subsidence variability. Water discharge and sediment flux sources in the model are defined parallel with and perpendicular to the strike of the half-grabens close to the corner of the model by a km-scale channel.

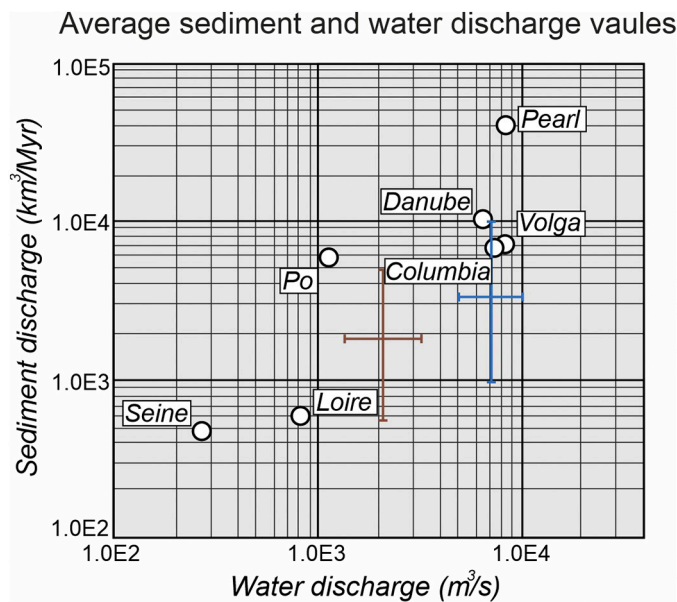


Fig. 2. Relation between sediment and water discharge based on observations from major rivers (modified after Csató et al., 2014). Brown and blue signs indicate values used in our stratigraphic forward modelling in dry and wet climatic scenarios, respectively. (For interpretation of the references to colour in this figure legend, the reader is referred to the web version of this article.)

during the subsequent post-rift phase. The Winkler’s hydrostatic pliable condition is set for the bottom boundary. We set 10 °C at the surface, 1300 °C at the base of the lithosphere and 1650 °C at the base of the model. The lateral thermal boundary condition includes zero heat flow. Detailed description of this numerical approach is further described in prior studies (Burov and Poliakov, 2003; Burov and Yamato, 2008; Francois et al., 2013).

2.2. Thermo-mechanical model setup

The three thermo-mechanical simulations (Figs. 3–4, 6) presented in this study (Table 1, for further model results see Appendix A) are based on previous parametric studies on lithospheric extension (Balázs et al., 2017a). The models show the extensional reactivation of a lithospheric-scale suture zone, which results in the formation and evolution of asymmetric extensional sedimentary basins.

We have defined a reference model (Fig. 3), which consists of a 135 km thick lithosphere including 20 km thick upper crust and 20 km thick lower crust and 95 km thick dry olivine lithospheric mantle overlying further 315 km asthenosphere of wet olivine rheology. The syn-rift phase is simulated by divergent velocities for 7.2 Myr followed by post-rift phase until 18 Myr numerical time. This model is compared to another experiment with a lower diffusion coefficient (250 m²yr⁻¹) simulating a more arid climatic condition. Furthermore, one additional experiment is conducted in the absence of surface processes (i.e., 0 diffusion coefficient). The initial Moho temperature is 725 °C. The crust is thinned by a factor of 2.5 in the basin centre. All these values resemble the syn- and post-rift evolution of the Pannonian back-arc basin (Horváth et al., 2015). Furthermore, in all models we defined a tilted rheological weak zone in the mantle lithosphere representing a suture inherited from a former subduction and orogenic episode. It is assumed that such former subduction and collision phase have resulted in a thickened crust and have released fluids during subduction creating the weak zone of wet olivine rheology in the lithosphere (Fig. 1). Such a heterogenous mantle is also described by geochemical studies from the Pannonian Basin (e.g., Harangi et al., 2001; Liptai et al., 2018). Further rheological, kinematic and geometrical parameters were tested in a similar previous study (Balázs et al., 2017a). These initial rheological and thermal parameters are designed to simulate a young orogenic structure preceding its extensional collapse. Rheological decoupling of the crustal and lithospheric layers takes place in most cases and results in horizontal ductile flow in the intermediate or lower crust (Burov and Poliakov, 2003).

Table 1

Basic parameters of the thermo-mechanical numerical experiments. Rheological parameters are adapted from similar numerical experiments (quartz-rich upper crust; diabase lower crust; dry and wet olivine mantle: e.g., Burov and Poliakov, 2003).

Length of model x_l	1000 km				
Amount of extension	150 km				
Extension velocity	2 cm/yr				
Vertical resolution in the upper crust	1.2 km				
Horizontal resolution	2 km				
Temperature at the base of the lithosphere	1300 °C				
Radioactive heat production, H_s	$1.5 \times 10^{-9} \text{ W kg}^{-1}$				
Radiogenic production decay length, h_r	10 km				
Upper crustal thermal conductivity, k_c	$2.5 \text{ W K}^{-1} \text{ m}^{-1}$				
Lower crustal thermal conductivity, k_c	$2 \text{ W K}^{-1} \text{ m}^{-1}$				
Mantle thermal conductivity, k_m	$3.3 \text{ W K}^{-1} \text{ m}^{-1}$				
Thermal diffusivity of mantle, χ	$10^{-6} \text{ m}^2 \text{ s}^{-1}$				
Specific heat, C_p	$1000 \text{ J K}^{-1} \text{ kg}^{-1}$				
Cohesion	20 MPa				
Byerlee’s law friction angle	30 °				
Initial surface heat flow	70 mW/m²				
Lamé elastic constants	30 GPa				
2D erosion coefficient in dry and wet climatic scenarios, k_{ero}	0 & 250 & 750 m² yr⁻¹				
	Upper crust	Lower crust	Mantle lithosphere	Weak zone	Asthenosphere
Thickness (km)	20	20	95	–	315
Density, ρ_0 (kg m⁻³)	2750	2900	3330	3270	3330
Power law constant, A (MPa ⁿ s⁻¹)	6.7×10^{-6}	6.3×10^{-2}	7×10^3	6.8×10^3	7×10^3
Creep activation energy, E (kJ mol⁻¹)	156	276	520	276	510
Power law constant, n	2.4	3.05	3	4	3

2.3. Stratigraphic numerical modelling method

DionisosFlow (Granjeon and Joseph, 1999; Granjeon, 2019) is a 3D deterministic diffusion-based model that accounts for the spatial and temporal variation of accommodation, water discharge, sediment supply composed of different sediment classes, compaction, eustasy and different erosion and sediment transport processes. Building on the tectonic subsidence history computed by the thermo-mechanical models the subsequent stratigraphic forward numerical modelling enables the analysis of sedimentary facies distribution, the evolution of the overall sedimentary transport routes and the basin-scale sedimentary architecture during the syn- and post-rift phases of basin evolution.

The physical equations are solved using a finite-volume implicit numerical scheme (Gervais and Masson, 2008). The set of nonlinear sediment production and transport equations is solved using a Newton algorithm. The model combines empirical water and gravity-driven diffusion equations, which include a slow long-term gravity-driven creeping law and a faster water-driven and slope-driven diffusion equation (Granjeon, 2019) leading to the following non-linear sediment transport equation:

$$Q_{s_i} = K_{s_i} S + K_{w_i} \hat{Q}_w^m S^n, \text{ where } \hat{Q}_w = Q_w / Q_{w_0} \quad (2)$$

where Q_{s_i} is the flux of the i -th sediment class [m^2s^{-1}], K_{s_i} is a creeping diffusion coefficient, S is the local slope gradient, K_{w_i} is a water-driven diffusion coefficient, \hat{Q}_w is a local normalized water discharge with $Q_{w_0} = 1 \text{ m}^3\text{s}^{-1}$, m and n are power coefficient constants with values between 1 and 2 (Tucker and Slingerland, 1994).

This transport equation reflects the overall sedimentary processes during erosion, transport and deposition at basin scale (Burgess et al., 2019). In classical landscape evolution numerical models, fluvial water flow is modelled using a single-direction routing method, where water flows towards the steepest slope (Tucker and Slingerland, 1994). The approach of DionisosFlow is different by simulating the behaviour of the entire sedimentary basin system at a larger scale. This regional approach uses a multi-direction method (Granjeon, 2019), where water is routed to all local lower neighbours of a given cell following slope ratios, which handles better diverging flow pattern (Tucker and Hancock, 2010) and is well adapted to simulate overland sheet flow as well as braided systems. Sedimentation and erosion rates for each sediment fraction at each cell are computed from the mass conservation equation and the actual sediment flux.

Accommodation space is controlled by the basement subsidence and eustatic sea-level variations. DionisosFlow can handle different synthetic or published eustatic curves. Further seasonal variability and climatic events are simulated by a statistical approach. Sediment transport is divided into short-term high-energy (HEST) and long-term low energy (LELT) intervals. This modelling approach assumes that during each time step a specific percent of the sediments are discharged by a much higher water flow rate simulating scarce, but extreme floods events (Granjeon, 2019). Building on a previous parametric study we set 33% of the sediments with 18 times higher water discharge value for HEST events resulting the most realistic facies distribution (Balázs et al., 2017b).

2.4. Stratigraphic model setup

The model setups are designed with and without along strike subsidence variability (geometry I and II in Model M1wet and M1dry respectively) and during wet and dry climatic conditions (Table 2). Basement geometries and subsidence rates derive from the thermo-mechanical simulations, where sediment transport is characterized by lower and higher diffusion coefficients simulating dry and wet climatic conditions (Fig. 4). Note that the different diffusion coefficients in the thermo-mechanical models resulted in different subsidence and uplift histories (Fig. 4) due to differences in strain localization, different sediment loading and unloading effects and different thermal evolution (Balázs et al., 2017a). The stratigraphic models simulating wet climatic conditions (Models M1wet and M2wet) are characterized by higher erosion rates, higher water and sediment discharge values and higher HEST/LELT discharge ratios (Table 2).

We defined an area of $150 \times 120 \text{ km}^2$ representing the most extended parts of the western Pannonian Basin, i.e., the Danube Basin (Sztanó et al., 2016) hosting the deepest (half)grabens with 2.5 km horizontal grid spacing (Fig. 1b). The external sediment and water sources are defined at the sides of the model close to the model corner, representing a kilometre-scale channel (Fig. 1b). External sediment supply and water discharge (Table 2) values laterally decreases from the centre of this channel towards its side. These sediment and water discharge values are derived from observations from natural examples, such as the Danube or Volga river deltas (Fig. 2). Simulations handle three sediment classes, such as mud, sand and basement derived cobbles, characterized with distinct diffusion coefficients (Table 2). The sediments are then transported towards the depocenters based on Eq. (2). Each model voxel is

Table 2
Main parameters of the four presented 3D stratigraphic forward numerical experiments. For further details see Granjeon (2019).

Horizontal model dimension	150 km × 120 km					
Horizontal model resolution	2.5 km					
Vertical resolution	variable ~1–100 m					
Water flow exponential, m	1.5					
Slope exponential, n	1.3					
External source sand/mud ratio	3/7					
Sediment class	Basement	Sand	Mud			
Grain size [mm]	4	0.25	0.0035			
Gravity-driven coefficient [km^2/kyr]	0.01	0.03	0.03			
Water-driven continental coefficient [km^2/kyr]	80	80	160			
Water-driven marine coefficient [km^2/kyr]	0.08	0.08	0.8			
Experiment	Max. syn- and post-rift basement subsidence	Maximum erosion rate	Maximum sediment supply	Maximum long-term water discharge	Short-term / long-term discharge ratio	Along-strike Geometrical variability
M1wet	4.25 km, 2 km	300 m/Myr	9000 km^3/Myr	2000 m^3/s	18	no
M1dry	3.25 km, 1 km	200 m/Myr	6000 km^3/Myr	1000 m^3/s	12	no
M2wet	4.25 km, 2 km	300 m/Myr	6000 km^3/Myr	2000 m^3/s	18	yes
M2dry	3.25 km, 1 km	200 m/Myr	4000 km^3/Myr	1000 m^3/s	12	yes

built up by the mixture of these classes that are visualized by their proportion. Compaction of sediments is computed following generic lithology-dependent porosity-depth curves (Appendix B). Additional internal sediment sources are the eroding basement rocks. Low amplitude climate-driven water-level variations are implemented by a sinusoidal function of 36 m half-amplitude and 300 kyr time period.

2.5. Model visualization

Thermo-mechanical model results are illustrated by phase composition, i.e., sediments deposited in the half-grabens, upper and lower crustal and lithospheric layers (Figs. 3–4). Finite strain and strain rate results illustrate brittle faults in the upper crust and ductile shear zones

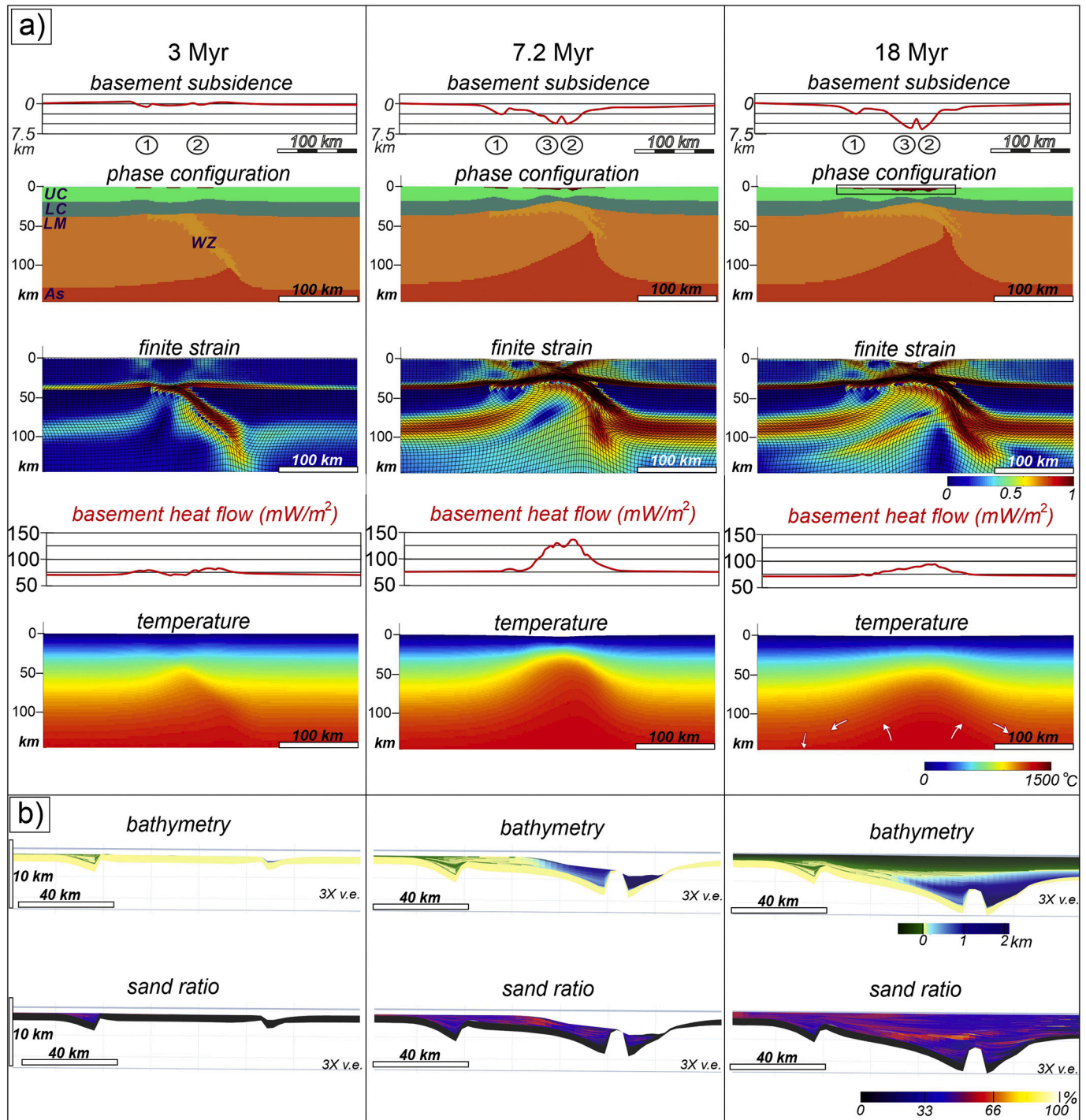


Fig. 3. The tectonic (a) and stratigraphic (b) evolution of the reference model simulating wet climatic condition, i.e., with high erosion and sediment flux values. Results during the syn-rift (3 Myr), at the transition from syn- to post-rift times (7.2 Myr) and after further 10.8 Myr post-rift evolution. Numbers above the phase configuration results show the gradual opening of the sedimentary subbasins. Depocenters are filled by sediments (red colour). UC – Upper crust, LC – Lower crust, LM – Lithospheric mantle, As – Asthenosphere, WZ – mantle weak zone. The basement subsidence pattern extracted from the thermo-mechanical experiment is used as input in the stratigraphic model. Bathymetry and sand ratio results are shown in cross sections through the centre of the 3D model. Note that thick sand bodies deposit in the topsets and in the uppermost part of the foresets of the prograding shelf-margin slopes and further sand portions are also transported at ~40 km distance from the shore. (For interpretation of the references to colour in this figure legend, the reader is referred to the web version of this article.)

in the middle and lower crust and in the mantle (Figs. 3–4). Basement subsidence curves (Fig. 4a) are calculated based on markers in the upper crust beneath three distinct half-grabens.

Stratigraphic models are illustrated by distinct output attributes. First, bathymetry images (Figs. 3–5, 7–9) represent the water depth of the sediments at the times of deposition. Sedimentation and erosion rates are extracted (Fig. 4) and the high energy water flux indicates the main sedimentary transport routes (Fig. 5). Furthermore, each model voxel is built up by the mixture of mud, sand and basement derived cobble classes that are visualized by their proportion (Figs. 3b, 9). Based on these attributes, we differentiated between small-scale coarse-grained deltas on the shelf, sandy lobes in the basin, footwall derived fans in the footwall proximity, and large-scale dominantly muddy shelf-margin slope sedimentation connecting the sandy-muddy shelf and the deep basin. The evolution of basement subsidence was obtained from backstripped well data from various sub-basins of the Pannonian Basin (Fig. 10), which are compared to our simulated basement subsidence data (Fig. 11).

Synthetic seismic sections are calculated by DionisosFlow based on the stratigraphic model results (Fig. 9) and compared with industrial reflection seismic profiles (Figs. 12–13). Densities and seismic velocities are assigned to each sediment classes. Sediment properties are refined by a maximum thickness of 60 m. Seismic impedance and reflection coefficient grids are calculated based on the calculated lithology grid (Appendix B). Each seismic trace is computed following the 1D convolution model between the reflection coefficients and a zero-phase Ricker seismic wavelet with 40 Hz dominant frequency and 2 msec sampling rate.

3. Model results

3.1. Thermo-mechanical reference model results

The reference model (Fig. 3) during the first 2 Myr of extension shows distributed low offset upper crustal faulting and rapid lithospheric mantle thinning due to strain localisation along the lithospheric weak zone. Further extension results in strain localisation in the crust above the weak zone leading to the formation and subsidence of distinct half-graben depocenters and uplift of their footwalls. The first two half grabens form near the margin of the underlying suture zone, while younger structures form towards the centre of the basin system. Subsidence rates of the syn-rift depocenters show notable spatial and temporal variation (Fig. 4). The first depocenter records 1 km/Myr initial subsidence rate for 1 Myr, followed by 0.3 km/Myr for 3 Myr and a final 0.6 km/Myr rate for additional 2.5 Myr. The second depocenter records an initial 0.5 km/Myr subsidence rate for 2.5 Myr and a faster 1.5 km/Myr subsidence for 2.5 Myr. The third, youngest depocenter also shows a three-stage subsidence pattern of 1.25 km/Myr rate for 1.2 Myr followed by a slower subsidence of 1 km/Myr for 1 Myr and a final 1.8 km/Myr subsidence rate. The upper crustal thinning is accompanied by ductile lower crustal horizontal shearing. Because localized brittle faults are accompanied by doming of the underlying ductile crust, domains of high upper crustal thinning have a thick lower crust (Fig. 3). The rapid asymmetric rise of the asthenosphere is associated with advective redistribution of the weak suture zone beneath the crust, which localizes deformation and controls the migration of extensional deformation from the margins towards the basin centre. This asymmetric rifting thins the crust from the initial 40 km to 17 km and the lithospheric mantle from 95 km to 30 km. After 7.2 Myr the extensional velocity is set to zero simulating the termination of syn-rift extension.

After the cessation of extension, the asthenospheric upwelling is attenuated to a more symmetrical geometry controlled by an overall post-rift cooling in the centre and by the development of small-scale convective cells beneath the basin margins. The lateral heat transport from the asthenosphere anomaly contributes to the uplift and erosion of the basin margins. Sediments are gradually re-distributed in the basin

centre resulting in elastic bending of the extended weak lithosphere (Figs. 3, 4). This mechanism enhances differential vertical movements during the “post-rift” phase. In fact, the oldest depocenter during the post-rift phase records slow uplift. In contrast, the basin centre records thermal subsidence with a rate gradually decreasing from 0.3 km/Myr at the onset of post-rift subsidence to 0.15 km/Myr at 18 Myr.

3.2. Thermo-mechanical parameter tests

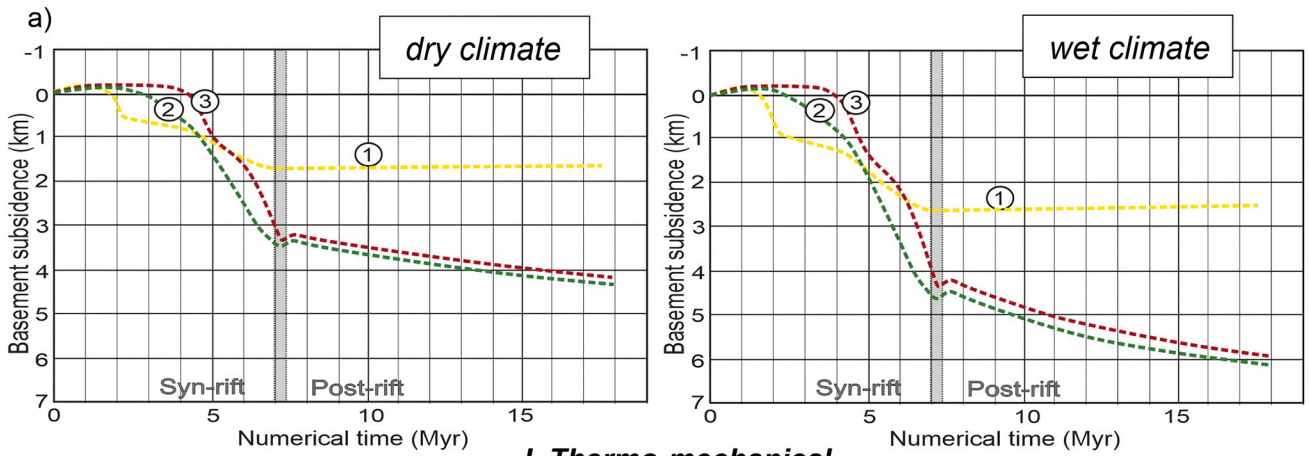
The model with lower erosion and sedimentation coefficient ($250 \text{ m}^2 \text{ yr}^{-1}$) shows an overall similar tectonic evolution to the reference model, however, strain localization occurs at different times and locations (Fig. 4). The first half-graben forms from ca. 1.75 Myr in both experiments, but the second and third half-grabens forms 0.5–1 Myr later in the experiment with lower erosion coefficient than in the reference model. A lower erosion coefficient implies lower erosion values of the basin margins that decreases the width of the depocenter by ca. 25 km, which is in agreement with previous studies (Burov and Poliakov, 2003). The lower erosion and sedimentation coefficients create more distributed deformation and a greater distance between the second and third half-grabens depocenters (40 km, Fig. 4). In this setup ductile shearing of the lower crust is suppressed beneath the main depocenters, thus brittle deformation is more dominant (Figs. 4b,c). Furthermore, the depocenters record lower subsidence rates during both syn- and post-rift times (Fig. 4). The first depocenter records subsidence rates of 0.8 km/Myr, 0.2 km/Myr and 0.4 km/Myr for 1 Myr, 3 Myrs and 2.5 Myrs, respectively. The second half-graben indicates an initial slow subsidence rate of 0.5 km/Myr for 2.5 Myrs, followed by 1.1 km/Myr subsidence rate for 3 Myrs. Finally, the third depocenter shows 1 km subsidence for 1 Myr, 0.6 km/Myr for 1 Myr and a final subsidence rate of 1.5 km/Myr until the end of the syn-rift extension. Post-rift times show slow uplift of the oldest depocenter, while half-grabens in the basin centre record post-rift subsidence with an initial rate of 0.2 km/Myr (Fig. 4).

3.3. Basin thermal history

The evolution of the basement heat flow is extracted from the uppermost upper crustal (basement) nodes based on the product of thermal conductivities and thermal gradients (Figs. 3, 6). The basement heat flow evolution of the reference experiment is shown 3 Myr after the onset of extension, at the end of the syn-rift extension at 7.2 Myr and during the post-rift phase at 18 Myr (Fig. 3a). The initial 70 mW/m^2 heat flow increases to 79 and 83 mW/m^2 in the close vicinity of the exhumed footwalls of the first two half-grabens by 3 Myr. By the end of the syn-rift phase maximum basement heat flow is recorded in the half-grabens above the elevated asthenosphere reaching maximum values of 126 and 139 mW/m^2 . In the first half-graben the heat flow value is only 77 mW/m^2 . During the post-rift phase the basement heat flow is gradually decreasing in the entire model domain, by 18 Myr, one large wavelength (ca. 125 km wide) elevated heat flow anomaly is shown, its maximum is 91 mW/m^2 (Fig. 3).

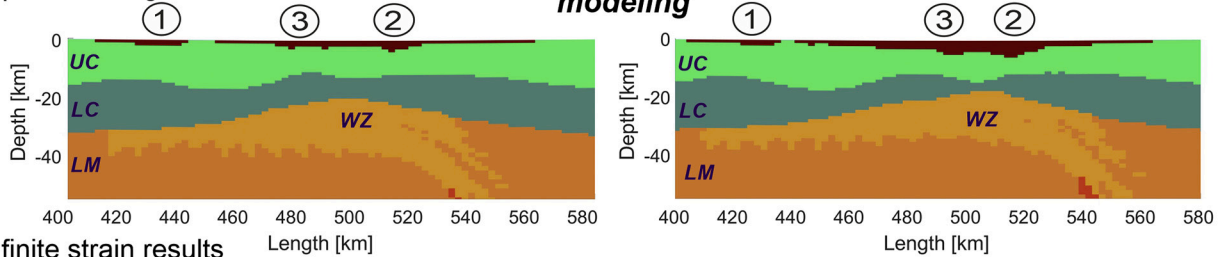
3.4. Stratigraphic reference model results

The reference stratigraphic model (model M1wet) shows the large accommodation space created in the first half-graben during early syn-rift evolution (Figs. 3, 5). This subbasin is fed by the external sediment source defined at the model boundary creating alluvial to shallow delta deposits of 1 km thickness (Fig. 3b). Footwall derived fans are deposited at the proximity of its boundary fault with decreasing sedimentation rate through time. From 3 Myr the second half-graben records greater subsidence rates leading to rapid transgression and greater water depth of 800 m. The water depth in the first half-graben increases to 400 m and subsequently decreases to a few tens of meters due to fast sedimentation (Fig. 5a). From 4 Myr the third subbasin evolves in

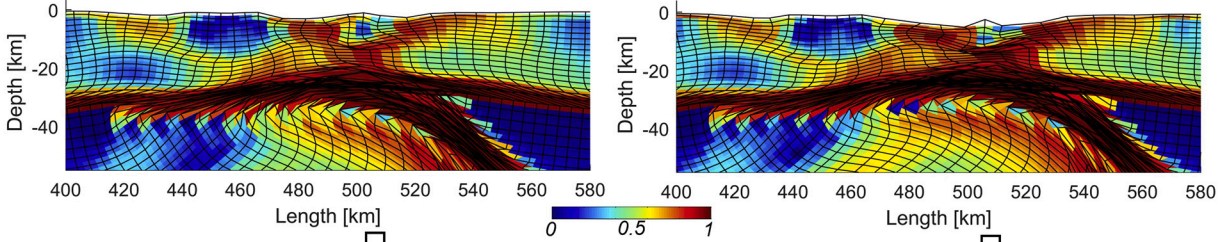


I. Thermo-mechanical modeling

b) phase configuration

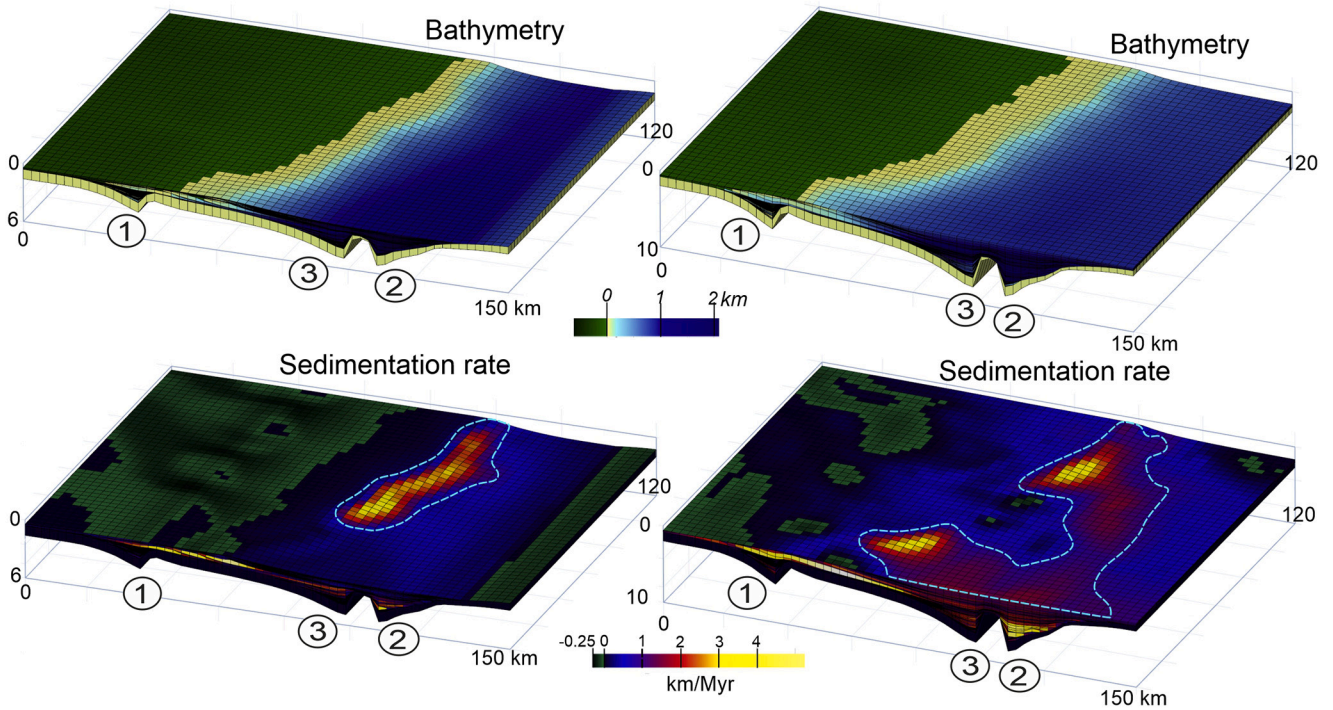


c) finite strain results



II. Stratigraphic modeling

d) Stratigraphic model results during late post-rift times



(caption on next page)

Fig. 4. Comparison of model results simulating dry (model M1dry) and wet (model M1wet) climatic conditions by implementing different erosion and sedimentation rates in both the thermo-mechanical and stratigraphic models. (a) Basement subsidence curves are extracted from the thermo-mechanical simulation from the three depocenters. (b-c) Phase configuration and finite strain results of the thermo-mechanical models. Note that higher diffusion coefficient and thus higher erosion rate creates an overall wider basin system and larger basement subsidence in the depocenters and higher exhumation rates of its margins. White lines are isotherms. (d) Bathymetric and sedimentation rate results during the post-rift phase (at 10 Myr) in the two climatic scenarios of the stratigraphic models.

between the first two (Figs. 3, 5b), which traps sediment arriving from the external source. This trapping basin and the uplifted footwall prevent sediment bypass to the third depocenter creating a starved basin that is solely sourced by its eroding footwall from this time. By the end of syn-rift times at 7.2 Myr the first half-graben is filled mostly by shallow water deltas. Deep water sediments are deposited for a short interval between ca. 6–7 Myr, when subsidence rate culminated in this area. In the most distal position from the source the second subbasin shows open-water sedimentation during the late syn-rift phase reaching a maximum water depth of 2 km (Fig. 3). The separating footwall in the middle of the model area has gradually subsided beneath water-level already during the syn-rift phase and from 6 Myr high energy currents simulating turbiditic currents have reached the second depocenter (Fig. 5c). Our imposed eustatic water-level variation was mostly overwritten by tectonics during the syn-rift phase.

At the beginning of post-rift evolution ca. 1–1.75 km water depth has been inherited from the preceding syn-rift subsidence for the second and third depocenters (Fig. 3), while the first half-graben area only records alluvial deposition (Fig. 5). This water depth has gradually decreased due to progradation of a large delta and shelf-margin slope system (Fig. 5). Coarse-grained sediments are deposited on the shelf and at the toe of the slope, while the shelf-margin slope remains mainly fine-grained (Fig. 3). Sand lobes are transported at larger distances during periods of wet climate, when water discharge values are increased (Fig. 4d). During the post-rift progradation eustatic variations control the width of the shallow water shelf and the location of the active delta system. During water-level rise and high stand conditions the shoreline retrogrades, while during sea-level fall the delta system reaches the shelf-break (Fig. 7). Width of the shelf varies between ca. 5–40 km (Figs. 7, 8). Finally, between 7.2 and 12 Myr the shelf-margin slope system progrades ca. 100 km leading to alluvial sedimentation in the entire model domain (Figs. 3, 5).

3.5. Stratigraphic model results simulating different basement geometries and climatic conditions

In the dry scenario, the overall basin evolution is similar to the reference experiment, however a few noteworthy differences need to be highlighted. During the arid climate the shallow water shelf is much narrower, in this experiment it is only 5–25 km wide, and therefore the active delta on the shelf reach the shelf-break faster (Figs. 4d, 8). Furthermore, due to the lower water discharge and HEST values in this dry scenario the sediments are deposited in a closer proximity to the shelf edge, turbidity currents cannot source the more distal parts of the basin (Fig. 4d). The overall stacking pattern shows a simpler pattern of progradation and aggradation, lobe switching, autogenic processes and their resulted unconformities are much less frequent (Fig. 8).

In two further simulations (models M2wet and M2dry) basement subsidence and uplift rates varied along the strike of the structures during wet and dry climatic conditions, respectively (Fig. 1c). During the syn-rift phase the subsiding hanging walls and uplifting footwalls only cover 66% of the model width, the throw of the boundary normal fault decreases towards the model sides representing segmented structures. In this setup the sedimentary transport routes are more divided between the three depocenters (Fig. 5). During the first 3Myr coeval sedimentation occurred in the first and second half-graben, while in the reference model high sedimentation rate has been only recorded in the second subbasin after the more proximal first subbasin was entirely filled. (Fig. 5a,b). The youngest depocenter in the middle of the model

area also represents a trapping basin, but high energy currents reach the distal model area earlier due to the overspill point developed due to the segmented fault geometry, where deep-water currents can bypass (Fig. 5c). This results in lower water depth values by the end of syn rift times, reaching ca. 1.5 km. Post-rift evolution is influenced by inherited seafloor morphologies, which are balanced by open-water sedimentation and high energy currents by 11 Myr (Fig. 5d).

4. Discussion

4.1. Migration of deformation during asymmetric extension

The inherited lithospheric weak suture zone localizes extensional deformation in the form of a long living migrating detachment fault, creating dominantly asymmetric structures. During the asymmetric extension a spatial shift between the active crustal thinning and lithospheric thinning occurs (Lister et al., 1986; Le Pourhiet et al., 2004; Dias et al., 2015; Lescoutre et al., 2019). The rapid lithospheric mantle thinning facilitated by the inherited weak zone leads to none or moderate syn-rift subsidence during the first few million years of extension (Fig. 4). Subsequent localization of extension in the crust leads to the successive opening of half-grabens and syn-rift sedimentation in their hanging walls (Figs. 3–4). Migration of deformation is controlled by the asymmetric lithospheric thinning connected to the redistribution of the weak zone beneath the crust. The subsidence rate variations in the depocenters are controlled by the activity of the specific normal faults, migration of deformation and strain localization in a next depocenter and ductile shearing of the lower crust beneath the basins. Furthermore, a large wavelength slow subsidence is caused by crustal-scale flexure (Lankreijer et al., 1995) of the basin from the late syn-rift time. This subsides the previously uplifted footwall beneath water-level (Fig. 3).

In agreement with previous studies (Burov and Poliakov, 2003; Bialas and Buck, 2009; Olive et al., 2014; Hart et al., 2017; Andrés-Martínez et al., 2019), our models show that higher erosion and sedimentation rates lead to earlier localization of deformation from the preceding distributed faulting and stretching phase (Figs. 4, 6). Larger sedimentation rates lead to higher subsidence rates in the depocenters. The hanging walls and the lower crust records higher temperatures due to sediment blanketing. The hot and weak crust is more prone to lower crustal flow, enhancing the localization of deeper subbasins and modifying the fault spacing pattern and faulting duration in the specific half-grabens (Figs. 4, 6).

4.2. Post-rift lithosphere and basin evolution

A short-lived uplift at the onset of the post-rift evolution is created by the rapid cessation of extension. Subsequent post-rift basin subsidence rates are dependent on the inherited crustal and lithospheric thinning and the rate of erosion and sedimentation. The highest post-rift subsidence rate is recorded in the experiment with an initial thicker crust and during the highest erosion and sedimentation rates, reaching an initial 0.3 km/Myr value.

The basin margins including the oldest half-graben record slow uplift during post-rift times (Fig. 4). This is controlled by the interactions between active asthenosphere convection, erosional unloading of the basin margins, sediment loading and lower crustal flow beneath the depocenter and by the elastic flexure of the weak extended lithosphere. Our previous parameter test on this process inferred that higher erosion rates lead to higher marginal uplift rates between 30 and 90 m/Myr.

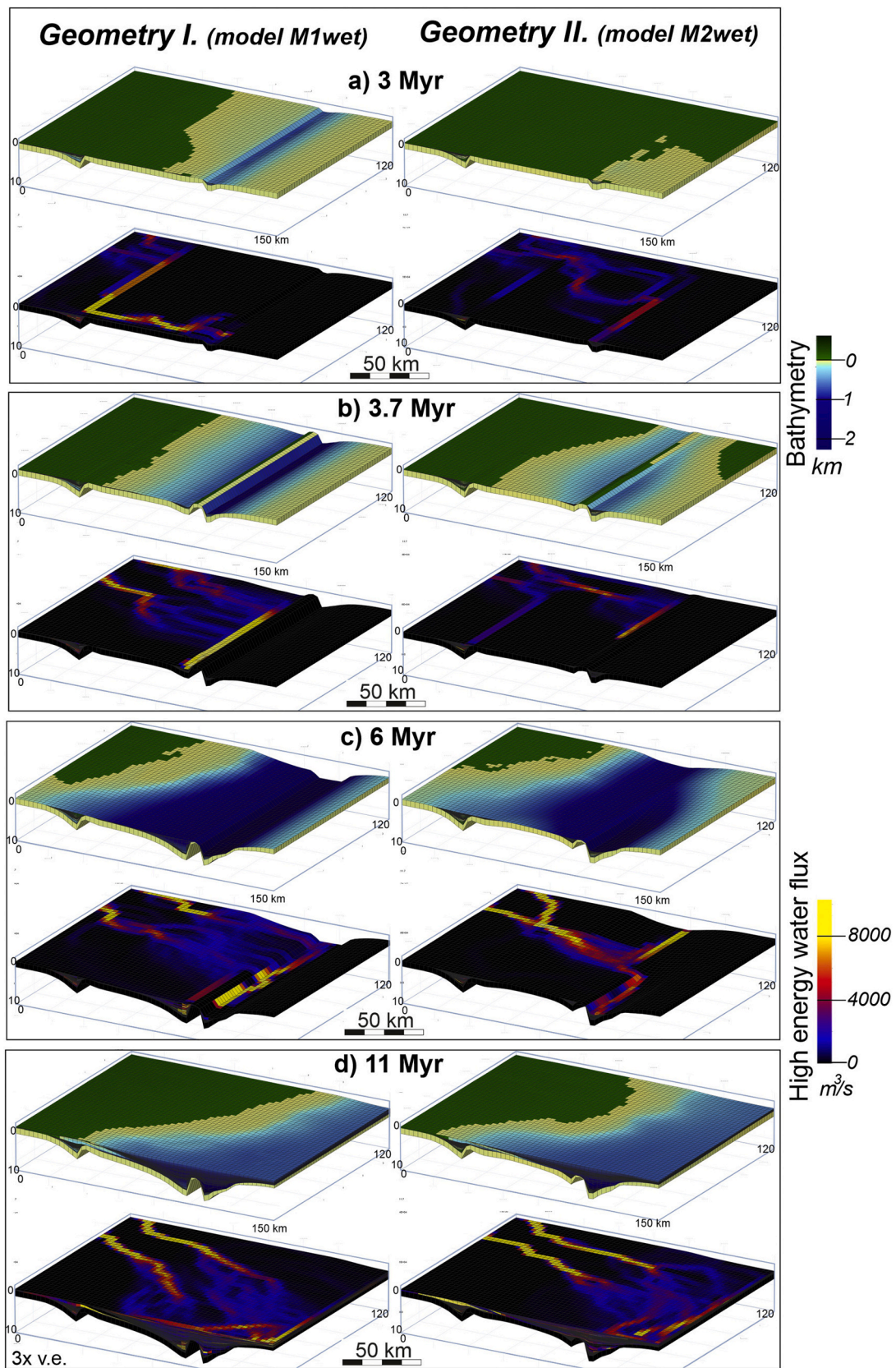


Fig. 5. Bathymetric and water flux evolution in the stratigraphic models without (Geometry I.) and with (Geometry II.) along-strike subsidence variability during wet climatic condition (models M1wet and M2wet, respectively). Note the sediment trapping in the middle depocenter at 3.7 Myr and the subsequent bypass through an overspill point from 6 Myr.

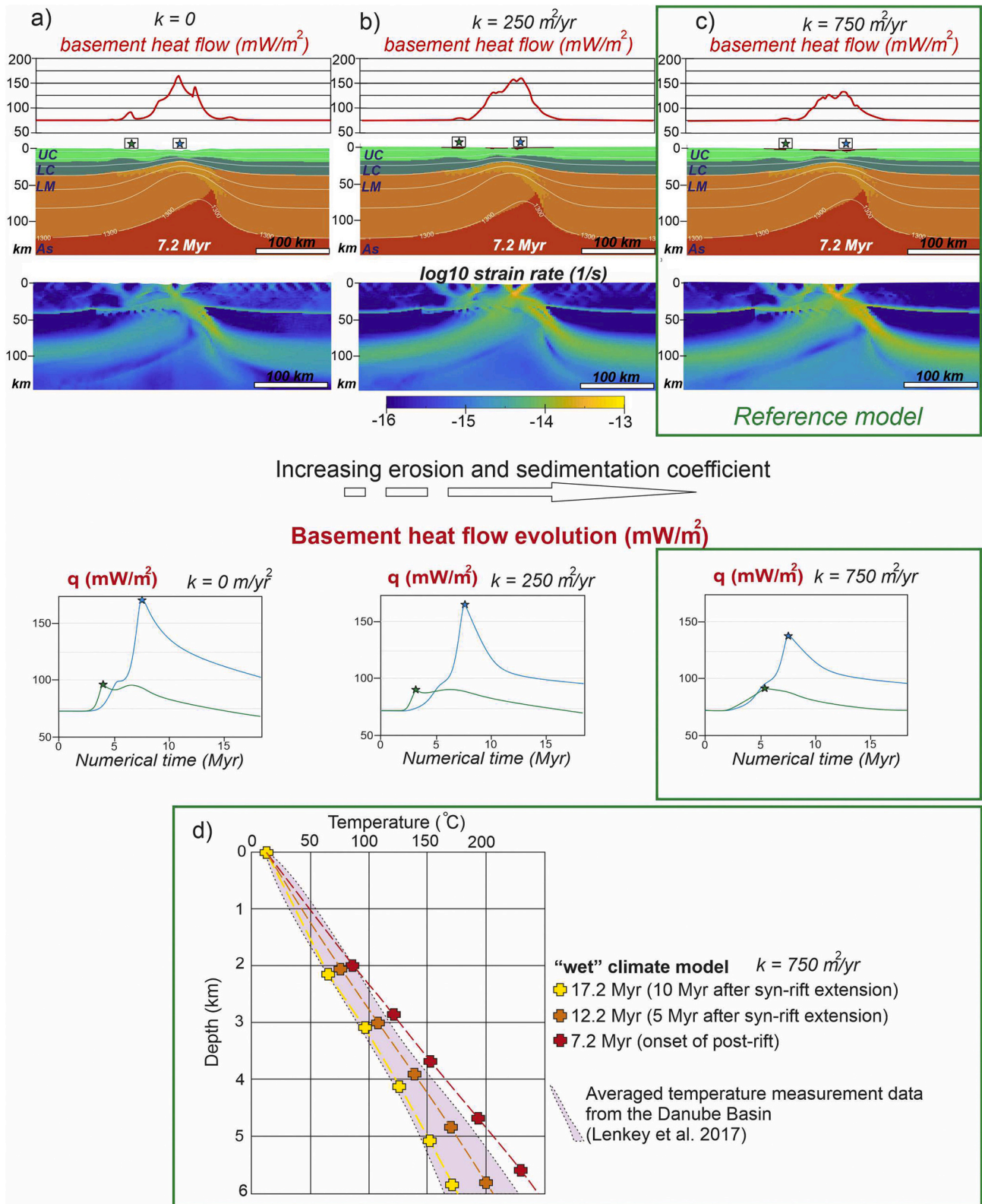


Fig. 6. The influence of surface processes on thermo-mechanical evolution. (a-c) Thermo-mechanical models with different diffusion coefficients shown after 7.2 Myr of extension. Higher rates of erosion and sedimentation result in a more efficient localization of deformation as shown by strain rate plots. Green and blue heat flow curves are extracted from the distinct half grabens as indicated in the phase configuration figures. Sediment blanketing causes smaller peaks of the heat flow values. UC – Upper crust, LC – Lower crust, LM – Lithospheric mantle, As – Asthenosphere, WZ – mantle weak zone. (d) Modelled temperature-depth profiles are compared with averaged temperature data from boreholes in the Danube Basin part of the Pannonian Basin (modified after Lenkey et al., 2017). (For interpretation of the references to colour in this figure legend, the reader is referred to the web version of this article.)

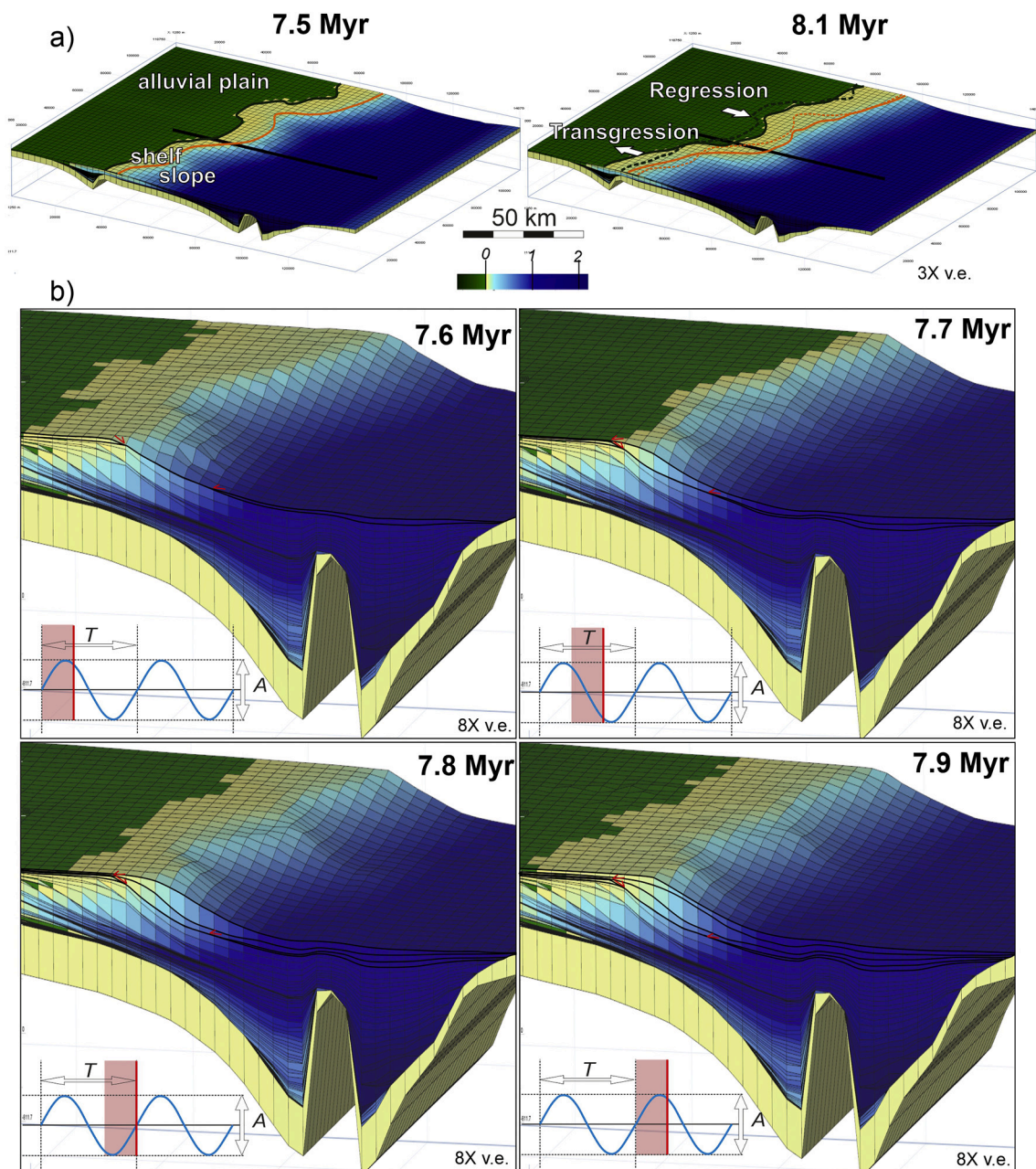


Fig. 7. Bathymetry figures inferring stratal stacking pattern during the overall late post-rift regression. Note the shoreline advance and retreat. (a) Oblique top-view figures show coeval transgression and regression due to laterally variable sedimentation rate. Green and orange colours indicate the shoreline and the shelf-edge at 7.5 Myr (left) and 8.1 Myr (right), respectively. Dashed lines in the right figure indicate the older lines correspond to 7.5 Myr (numerical time). (b) Zoomed figures indicate the stacking pattern and reflection terminations at different eustatic conditions. Note the difference between the shelf and the deep basin sedimentation during highstand and lowstand conditions. Thick clinoforms are built when the shelf is narrow and thus the delta system can feed the deep basin. (For interpretation of the references to colour in this figure legend, the reader is referred to the web version of this article.)

(Balázs et al., 2017a). By the end of syn-rift extension small-scale mantle convection cells are induced due to the high lateral temperature gradient between the elevated asthenosphere and the colder lithospheric mantle. Such convective cells effectively heat up laterally the lithosphere during the post-rift times, while the lithosphere beneath the depocenter cools down and subsides. Through time such convective cells can be even more pronounced leading to basaltic magmatism (Ballmer et al., 2010). In back-arc settings, due to the high extension rates (2–4 cm/Myr; Faccenna et al., 2014), the lateral temperature gradient and thus the convection is especially amplified. Similar small-scale convective cells are proposed for the case of passive margins (Buck, 1986; Ramsay and Pysklywec, 2011) or in different oceanic intraplate

settings (Ballmer et al., 2010).

4.3. Thermal evolution of sedimentary basins during the syn- and post-rift phases

The thermal gradient and thus basement heat flow increases due to the gradual upwelling of the underlying asthenosphere and conductive heat transport within the thinned lithosphere (Royden and Keen, 1980). This well studied mechanism is mainly affected by the initial crustal and lithospheric thicknesses and the rate and duration of extension (e.g., Theissen and Rüpke, 2010). This mechanism creates a large wavelength thermal anomaly and thus it decays within tens of millions of years

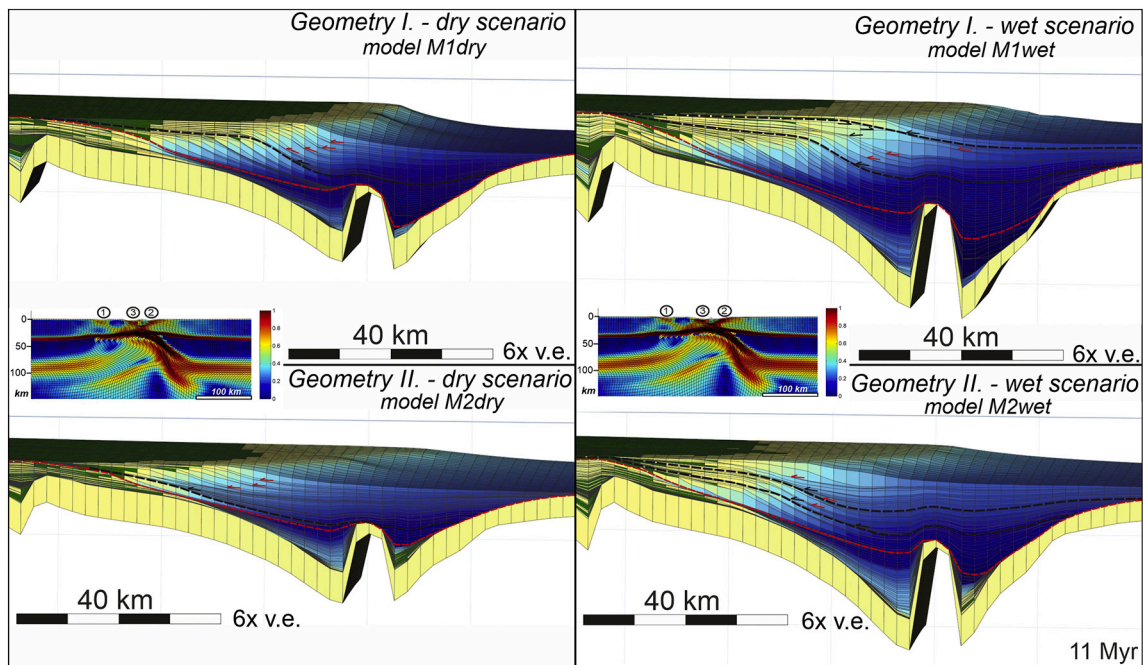


Fig. 8. Paleobathymetric evolution of the four presented stratigraphic numerical experiments shown at 11 Myr during the late post-rift period. Note the contrasting syn- and post-rift sedimentary thicknesses in the depocenters. Red unconformity indicates the termination of the syn-rift extensional boundary velocities applied in the thermo-mechanical models. Black unconformities bounded by coastal and marine onlaps indicate autogenic lobe switching events. Red arrows indicate marine onlaps caused by toe of slope turbidite lobes. Black arrows are reflection terminations caused by lobe switching. Note that in the wet scenarios due to the rapid subsidence, the rate of accommodation creation is much larger than the rate of sedimentation during water-level rise and thus 35 km wide transgression is recorded, while in the dry scenarios, where the subsidence rate is lower mainly normal regression and aggradation is recorded. (For interpretation of the references to colour in this figure legend, the reader is referred to the web version of this article.)

during post-rift times (e.g., Royden and Keen, 1980).

Localized crustal thinning and extensional exhumation of the footwalls of normal faults significantly increase locally the thermal gradient and the basement heat flow (Ter Voorde and Bertotti, 1994). The migration of active deformation and normal faulting from the periphery of the basin towards its centre controls the variation of the highest heat flow values within the basin system (Balázs et al., 2017a; Hart et al., 2017; Lescoutre et al., 2019). The resulted thermal anomalies have a much smaller extent and thus thermal equilibrium can be achieved within a few millions of years.

Surface processes in terms of footwall erosion and hanging-wall sedimentation also play a major role in the temporal and spatial evolution of basement heat flow (e.g., Hutchison, 1985). Erosion and sedimentation localize deformation (Burov and Poliakov, 2003; Bialas and Buck, 2009) and thus enhance crustal exhumation and lithospheric thinning and increase the heat flow. On the other hand, deposition of cold sediments and sediment thermal blanketing depresses the syn-rift and steady-state heat flow (Ter Voorde and Bertotti, 1994; Theissen and Rüpke, 2010).

In our reference experiment with a higher sedimentation rate, the top of the basement in the most extended domain records ca. 175 °C, while in the experiment with lower sedimentation rate the top basement records only ca. 110 °C by 18 Myr (Fig. 6). Note that the higher sedimentation rate leads to greater basement subsidence and more localized thinning and thus causes a higher temperature at the top of the basement, but the thermal gradient and thus the heat flow is lower. The interactions between all the above-mentioned processes lead to a non-monotonous evolution and major deviations from the classical basin modelling predictions (Royden and Keen, 1980). The basement heat flow decreases in the subbasins located at the margins, where deformation has ceased, while in the basin centres, the heat flow still increases until the end of the syn-rift period (Fig. 6).

Our numerical modelling results indicate a spatial and temporal shift

between the onset of extension, the onset of syn-rift sedimentation in specific half-grabens, the onset of increasing basement heat flow and the time of maximum heat flow values reached during basin evolution (Figs. 3, 4). Basement heat flow increases first in the oldest half-grabens that are often at the basin margins by the end of extension. Instead of a monotonous heat flow rise during the syn-rift and gradual decrease during the post-rift times, heat flow values record rapid increase periods during normal faulting superimposed on a large wavelength stagnation, fall or gradual rise depending on the location of lithospheric thinning (Fig. 4). Heat flow values start to decrease already during the syn-rift phase in subbasins, where normal faulting ceases and are in a distal position from the location of final lithospheric thinning. Sedimentation in depocenters also enhances lateral heat transport in the crust and thus our modelled heat flow curves are smoother. Sediment blanketing slows down the rate of post-rift cooling. During the post-rift phase the experiment without surface processes records the fastest cooling, the 200 mW/m² high heat flow value decreases to 110 mW/m² within 10 Myrs, while the experiment with the highest sedimentation rate records a much lower cooling rate from a maximum 145 mW/m² to 96 mW/m² (Fig. 6).

4.4. Tectonic and climatic controls on syn- and post-rift sedimentary architecture

Joint tectonic and stratigraphic modelling highlights the development of prograding-retrograding sedimentary cycles with different wavelength and temporal scales. The largest spatial scale characterizes the overall re-organization of the sedimentary system during the transition from syn- to post-rift evolution. The associated short-lived basin uplift creates a pronounced unconformity marked by erosional truncations of the underlying syn-rift strata and onlap and downlap terminations of the early post-rift sediments in the shallow water parts of the basins (Fig. 8). However, the second and third depocenters, located at

larger distances from the shoreline and thus recording high water depth, only record condensed pelagic sedimentation and inherit kilometre-scale bathymetry.

The basin-fill of the first depocenter indicates two tectonically-driven retrograding-prograding cycles during its syn-rift evolution (Fig. 3b), which corresponds to intervals of higher and lower subsidence rates coupled with a larger depositional rate during extension (Fig. 5a). This cyclicity is not visible in the second and third depocenters that were underfilled during their syn-rift evolution. Similar tectonically driven cyclicity has been reported from many extensional basins (Martins-Neto and Catuneanu, 2010; Andrić et al., 2017; Balázs et al., 2017b; Hou et al., 2020) connected to the peak activity of normal faults. Our modelling furthermore highlights, that depocenters located in a distal position from the sediment source can be underfilled for millions of years. This results that the tectonically driven transgressive-regressive cycles cannot be always detected in such starving syn-rift half-grabens. Nevertheless, opening of new sedimentary pathways by filling of an intervening trapping basin or opening of new gateways, can rapidly bring kilometre thick sediments following the preceding condensed sedimentary record (Fig. 6c).

In classical passive margin settings, the rate of eustatic variations usually outpaces the rate of tectonically induced motion, and therefore the balance between sedimentation rate and sea-level variations control basin architecture (Schlager, 1993; Henriksen et al., 2011). However, in rift basins or during the early post-rift phase of extensional back-arcs the high subsidence rates (Fig. 5) are often in the same order of magnitude as the climatically induced lake- or sea-level variations. This means that moments of base-level fall are hidden by the ongoing high subsidence and thus the spatial and temporal variation of subsidence still controls the stratal stacking pattern and shelf-edge trajectory, like in our wet scenario (Fig. 8). The superposition of the imposed base-level variation of ± 36 m and the modelled post-rift subsidence creates episodes of progradation and aggradation leading to stagnating and rising shelf-edge trajectories in our wet models, while in the dry models, where subsidence is lower, moments of forced regression are more visible (Fig. 8). This is further analysed in our reference model by showing different stages of the eustatic curve (Fig. 7). The joint effect of the post-rift subsidence and eustatic water-level rise creates longer periods with high increase rate of accommodation, thus transgression likely develops, while relative water-level fall and forced regression is suppressed or has shorter time intervals. Our experiments simulate the evolution of small-scale deltas prograding on the shelf and the progradation of the kilometre-scale shelf margin slope clinoforms (Fig. 11; Porebski and Steel, 2003; Sztanó et al., 2013). During highstands, there is a wider shallow water shelf area, where the active delta system has shifted landward, and deep-water lobes overlap the older shelf margin slope clinoforms (Fig. 8). A falling sea-level lead to regression, the active delta progrades basin-wards and creates thick clinothem foresets connecting the shelf and the deep basin. During lowstands, thicker foresets and bottomsets are deposited. Rising sea-level causes rapid aggradation and retrogradation of the clinoforms, while the delta is shifted landwards again over the shelf. A similar cyclicity was previously proposed for different passive margins or deep lacustrine shelves (Henriksen et al., 2011; Sztanó et al., 2013). Our experiments simulating more arid conditions infer a generally narrower shelf due to lower subsidence rates. Therefore, the rate of accommodation increase is lower. This condition enables the delta system located on the shelf to reach the shelf edge faster (Fig. 8).

Unconformities are also generated by autogenic processes (Fig. 8). Lateral migration of the active delta system on the shelf and lobe switching creates overlap surfaces without changing the subsidence rate or changing the externally defined water and sediment discharge (Balázs et al., 2017b; Burgess et al., 2019; Harris et al., 2020; Kovács et al., 2021). Our modelling also shows coeval transgression and regression controlled by the lateral variability of sedimentation rate along the shelf due to the migration of the delta system (Fig. 7a).

4.5. Comparison with observations from asymmetric extensional basins

The numerical models presented in this study can be compared with observations from highly extended asymmetric extensional basins dominantly sourced from one main direction, like in the case of many Mediterranean back-arc basins. The Pannonian, Aegean, Alboran and Liguro-Provençal–Thyrrhenian extensional back-arc basins accommodated the retreat of the Vrancea, Aegean, Gibraltar and Calabrian slabs during the formation of the Carpathians, Hellenides, Betics-Rif and Apennines orogens, respectively (e.g., Faccenna et al., 2014). Fast back-arc extension created a series of genetically linked half-graben geometries in the crust, and the thin lithosphere is associated with high heat flow values of ca. 80–145 mW/m² (Faccenna et al., 2014; Horváth et al., 2015).

Our modelled sedimentary architecture and unconformities can be compared to high resolution seismic images (e.g., Sztanó et al., 2013; Leroux et al., 2014; Milia et al., 2018; Balázs et al., 2018a). Our computed synthetic seismic sections (Fig. 9) show the characteristic seismic facies of the syn-rift depocenters and post-rift deep-water marls and turbidites, clinoforms and overlying delta and alluvial environments. The different marine or lacustrine sedimentary basins are characterized by different sediment and water discharge and different eustatic and water-level variations (Kováč et al., 2007; Gong et al., 2019), but our models provide insights into the formation of the observed sedimentary cycles and unconformities in these basins.

4.5.1. The evolution of the Pannonian Basin

The Pannonian Basin of Central Europe (Fig. 10) is a continental extensional back-arc basin, where the Miocene extension was mainly controlled by slab roll-back along the Carpathians (Horváth and Royden, 1981). Extension followed the Mesozoic opening and subsequent closure of the Alpine Tethys and the northern branch of the Neotethys oceanic realms (e.g., Csontos and Vörös, 2004). By the end of Paleogene times continental collision resulted in an orogenic area with thickened crust. The pre-Neogene basement of the present Pannonian Basin is composed of two distinct mega-units, i.e., the ALCAPA and Tisza-Dacia, with different paleogeographic positions, derived from the Alpine and Dinaridic orogenic systems (e.g., Csontos and Vörös, 2004). The two mega-units were affected by different extensional kinematics and coeval counter clockwise and clockwise rotations in ALCAPA and Tisza-Dacia, respectively, during their syn-rift evolution (Balla, 1987; Fodor et al., 1999; Kovács et al., 2007). Available estimates on the amount of extension are in the order of 150–250 km (Ustaszewski et al., 2010; Matenco et al., 2016; Balázs et al., 2018b). Both mega-units show the migration of extensional deformation from the basin margins and the formation of a series of half-grabens with variable subsidence rates (Fig. 1). The gradual Miocene subsidence of hanging-walls and the exhumation of footwalls in individual structures created an initial archipelago paleogeography in the larger Pannonian area (Nagyvarosy and Hámor, 2012; Pavelic and Kovacic, 2018). The last stages of major deformation and highest subsidence rates were recorded in the Danube Basin (Sztanó et al., 2016; Šujan et al., 2018) in the ALCAPA mega-unit, and in the central Great Hungarian Plain part of the Tisza-Dacia mega-units (Fig. 1; Tari et al., 1999; Balázs et al., 2018b).

Following a short-lived regional uplift event between the middle and late Miocene the Pannonian Basin was paleo-geographically isolated from the larger Paratethys realm that created a major environmental change and the birth of the endemic Lake Pannon (Magyar et al., 2013). The basin fill recorded an initial transgression followed by large-scale progradation over 400 km between 10 and 4 Ma from the NW and NE in a S-SE direction (Magyar et al., 2013). This progradation created a diachronous lithostratigraphy (Juhász, 1991; Sztanó et al., 2013) varying from alluvial and delta plain to open-water deposition, well constrained by reflection seismic data (Juhász, 1991; Pigott and Radivojević, 2010; Magyar et al., 2013; Balázs et al., 2018a).

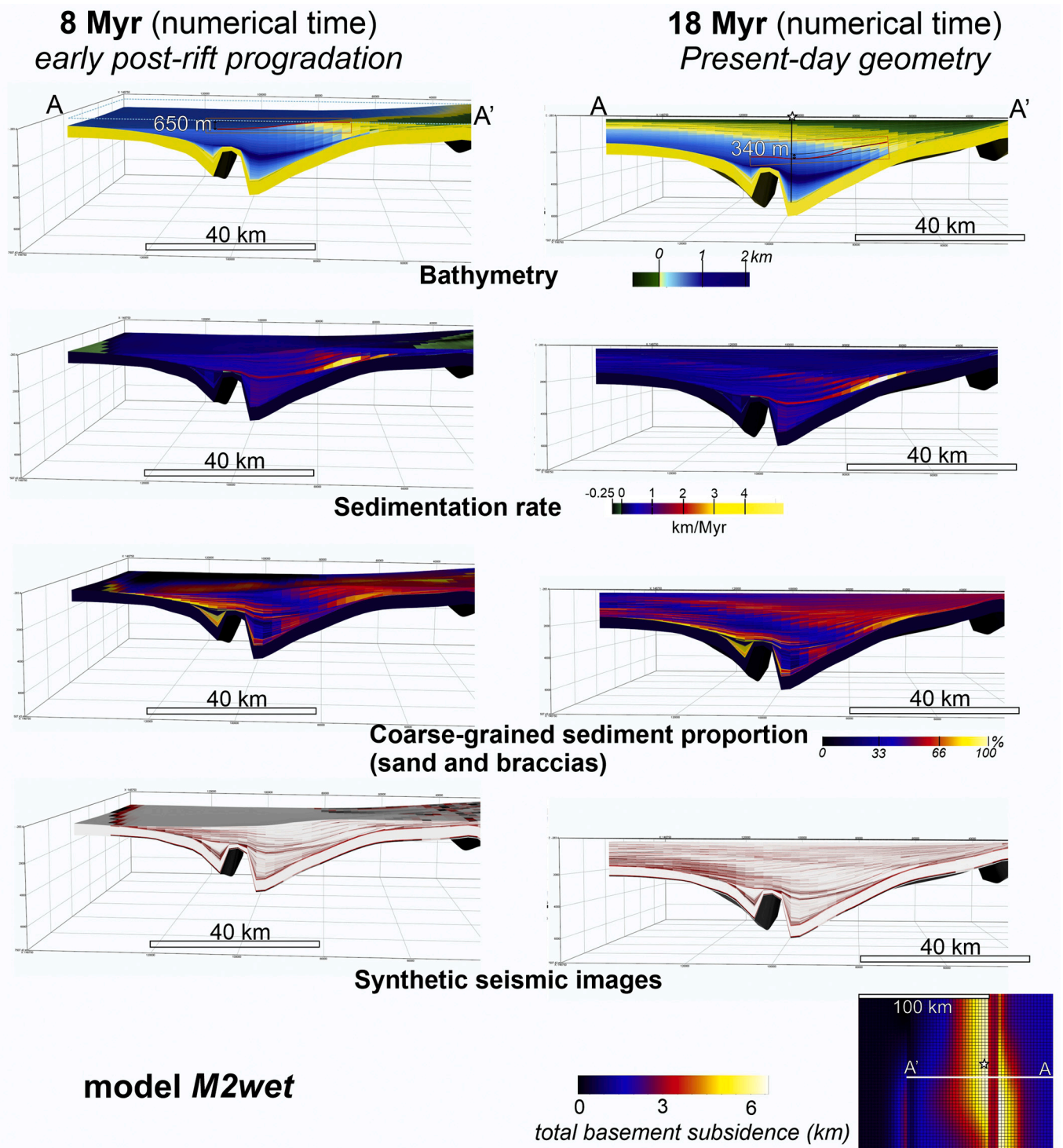


Fig. 9. Stratigraphic model results imposing wet climatic conditions and along-strike subsidence variations (model m2wet) during early post-rift times and at the end of the simulation. Compare the characteristic seismic facies units of the synthetic seismic data with the seismic section (Figs. 12–13) from the western part of the Pannonian Basin. Red line in the bathymetric figures indicate a shelf margin slope clinoform deposited at 8 Myr and subsequently deeply buried and compacted. Top right image shows the simulated well location of Fig. 11. (For interpretation of the references to colour in this figure legend, the reader is referred to the web version of this article.)

4.5.2. Model implications for the evolution of the Pannonian Basin

In the Pannonian Basin, in agreement with our modelling results, oldest early and middle Miocene depocenters are presently located at the periphery of the larger Pannonian Basin system, while the youngest and deepest half-graben geometries, such as the Makó Trough formed during early Late Miocene times in the centre of the Great Hungarian

Plain (Fig. 1). The older subbasins at the basin margins (Fig. 1), such as the Styrian Basin (Ebner and Saschenhofer, 1995), westernmost Danube Basin (Fig. 10) or the Miocene basins along the Transdanubian Range and North Hungarian Mountains, East Slovakian Basin or depocenters in the vicinity of the Apuseni Mountains all record present-day uplift (Dunkl and Frisch, 2002; Fodor et al., 2005; Ruzsiczay-Rüdiger et al.,

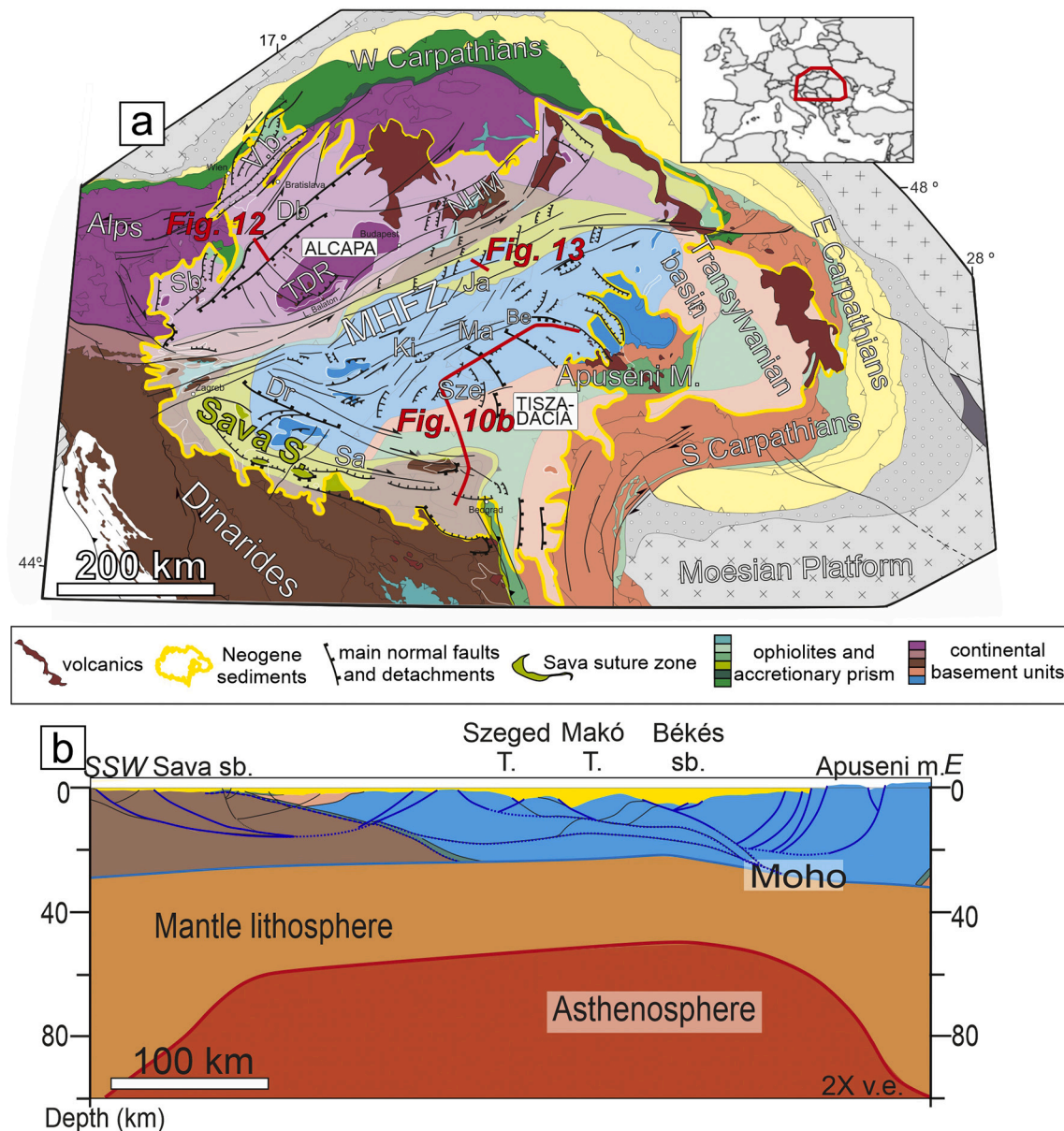


Fig. 10. (a) Tectonic map of the Pannonian Basin system, indicating the main Miocene extensional structures. Db = Danube Basin, TDR = Transdanubian Range, NHM = North Hungarian Mountains, Vb = Vienna Basin, Sa = Sava Subbasin, Dr = Dráva Subbasin, Ki = Kiskuhallas Subbasin, Ma = Makó Subbasin, Be = Békés Subbasin, Jászsag Subbasin, Sb = Styrian Subbasin, Sze = Szege Subbasin. Note the suture zones at the Dinaridic and Carpathian margins of the basin. Pre-Neogene basement map is modified after Schmid et al. (2008). (b) Interpreted composite section through the southern parts of the basin. Upper crustal geometry is based on seismic interpretation (cf. Balázs et al., 2017a). The Sava suture zone is mapped at the Dinaridic margin.

2005; Bada et al., 2007; Balázs et al., 2018a). The long-term post-rift uplift of the basin margins is caused in our models by the lateral heat transport from the asthenosphere upwelling and by lithospheric flexure due to sediment unloading from the margins and deposition in the basin centre (Balázs et al., 2017a). Sediment re-distribution also contributes to ductile deformation of the weak lower crust, locally accentuating differential vertical movements (Burov and Poliakov, 2003). This process is especially effective during wet climate (Fig. 5c). Uplift and erosional truncation of the late Miocene sediments at the basin margins (Fig. 10) and increased subsidence and sedimentation in the local depocenters (Sztanó et al., 2013; Horváth et al., 2015) are in good agreement with this proposed post-rift mechanism. In the case of the Pannonian Basin neotectonic inversion and positive reactivation of Miocene normal faults accentuates the uplift of the southwestern margins of the basin (Fodor et al., 2005; Bada et al., 2007).

Our modelled heat flow evolution (Fig. 4) takes into account the

large-scale lithospheric thinning and crustal scale thermal anomalies due to local normal faults and detachments during the syn-rift phase inferring a highly variable pattern in the different depocenters. Our reference model infers an exponential decrease from a maximum 150–140 mW/m² to the present-day values of ca. 80–110 mW/m² following post-rift cooling and the deposition of thick post-rift sediment. These values are in agreement with present-day temperature measurements from the Danube Basin part of the larger Pannonian Basin system (Fig. 4; Horváth et al., 2015; Lenkey et al., 2017).

Our stratigraphic model results of genetically linked half-graben depocenters and their sedimentation from one dominant direction shows a similar tectono-stratigraphic architecture to the Danube Basin area in the ALCAPA mega-unit in the West and with the Great Hungarian Plain in the Southeast parts of the Tisza-Dacia mega-unit (Fig. 10). Syn-rift depocenters that were located in the proximity of their source regions recorded high sedimentation, like the Zsira Trough (Fig. 12),

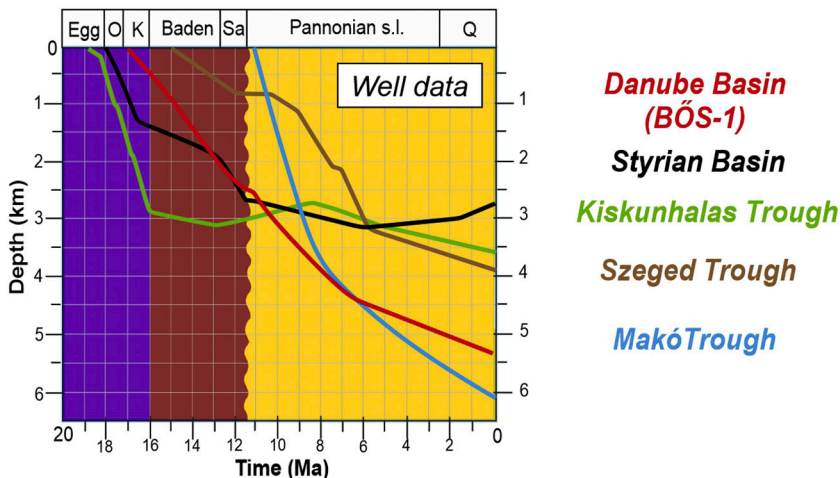
Kiskunhalas Trough or subbasins along the Dinaridic margin (Fig. 10). These depocenters show similar tectonics controlled transgressive-regressive cycles (Balázs et al., 2017b; Andrić et al., 2017) like our modelled cyclicity in the half-graben (no. 1 in Fig. 3). However, depocenters located at large distances from the main sediment sources during their syn-rift evolution, such as the late Miocene Makó Trough (Fig. 1) or the central Danube Basin were likely characterized by ca. 1.5 km paleobathymetry as sedimentation did not take pace with the fast subsidence during its rift climax (Sztanó et al., 2013; Balázs et al., 2017b). Nevertheless, cyclicity of the sedimentation rate is also predicted in all these situations (Fig. 11). In all these basins the exhumed footwall sources the neighbouring depocenters by coarse breccias during or after the activity of the boundary faults (Sztanó et al., 2013; Sebe et al., 2019). As the topographic high is progressively eroded, the sediments ultimately bypass and are deposited over the footwall. The models predict that the diachronous transition from syn- to post-rift times were associated with great water depth up to 1600 m in the depocenters, while the more proximal areas experienced exposure and erosion.

Our modelled progradation of large-scale shelf-margin slope clinoforms connecting the shelf and the deep basin and small prograding

deltas on the shelf is in agreement with observations from the Pannonian Basin (Csató et al., 2013; Magyar et al., 2013; Sztanó et al., 2013). The decompact height of these clinoforms is ca. 600–1000 m with a dip angle of ca. 3–8 degrees (Fig. 11; Balázs et al., 2018a) which is similar to our model result (Figs. 8–9). The maximum water depth was probably even higher in the most distal and continuously subsiding areas, such as the Danube Basin or Makó Trough, where deep water marl and turbidite deposition decreased the water depth from a maximum 1500 m below 1000 m (Sztanó et al., 2013; Balázs et al., 2017b). Sediment overburden and compaction of the slope sediment decreases their thickness from the maximum 1000 m to ca. 600 m (Figs. 9, 11). In the Danube Basin, the differential compaction decreased the clinoform height from 650 m to 340 m and created a folded geometry (Fig. 9). Our simulated periods of increased and decreased sedimentation rates resemble the initial pelagic or profundal environment, the subsequent events of turbidite lobes deposition and shelf-slope sedimentation and the final slowing of sedimentation in an alluvial environment (Fig. 11). Higher order sedimentation rate variation (Fig. 11) is connected to lobe switching events (see also Uhrin and Sztanó, 2011).

Finally, our modelled basin architecture shows the large-scale

a Backstripped basement subsidence curves from the Pannonian Basin system



b Backstripped basement subsidence curves from the numerical model (m2wet)

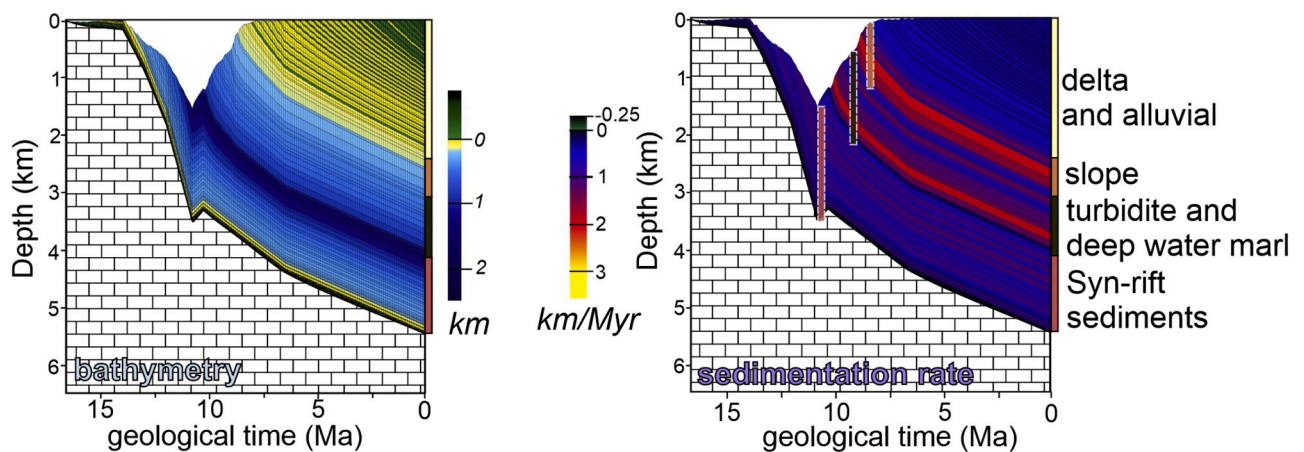


Fig. 11. (a) Backstripped well data, i.e., sediment loaded basement subsidence curves from different Pannonian Basin depocenters. (b) Sediment loaded basement subsidence curves from the numerical model m2wet from the centremost half-graben. For the simulated well location see Fig. 9. Note the original and compacted thickness of the stratigraphic units shown by the bars in the sedimentation rate figure.

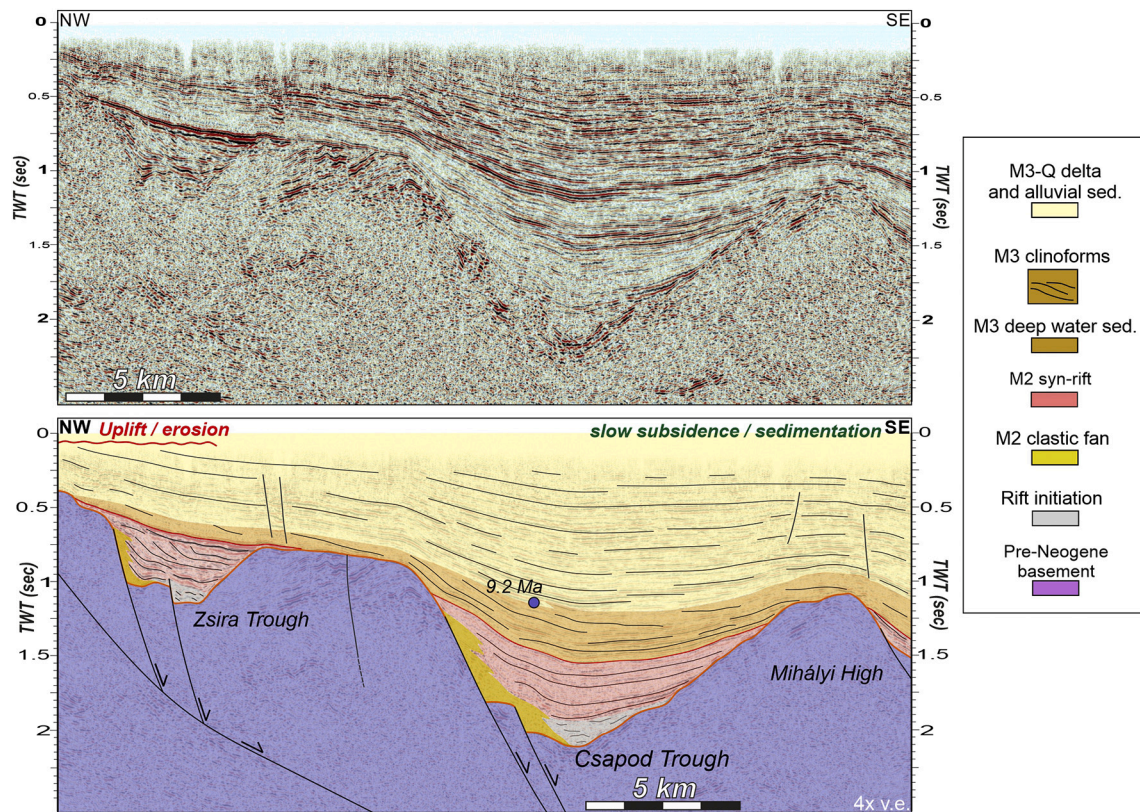


Fig. 12. Noninterpreted and interpreted reflection seismic section from the Danube Basin of the Western Pannonian Basin. For location see Fig. 1. Orange line indicates the base Neogene unconformity, red line indicates the base of the upper Miocene (Pannonian) sediments. (For interpretation of the references to colour in this figure legend, the reader is referred to the web version of this article.)

syncline geometry in the basin centre resembling the ongoing subsidence, gentle anticline geometries above buried footwalls created by differential compaction and erosional unconformities, together with thinning of the post-rift strata towards the basin margins controlled by their post-rift uplift (Figs. 9–11).

5. Conclusions

The joint thermo-mechanical and stratigraphic models provide insights into the links between lithospheric, asthenospheric and surface processes, such as erosion and sedimentation during asymmetric extension.

Strain localization and the shift from stretching and distributed faulting to enhanced and localized thinning and deep half-graben formation is facilitated by higher erosion and sedimentation rates. Subsidence rate and basement heat flow evolution of the depocenters show large variabilities during asymmetric extension. These values depend on their initial position from the inherited suture zone that controls fast lithospheric thinning and depend on the timing of crustal thinning caused by the migration of normal faulting. Sedimentation in their hanging walls localize deformation and sediment blanketing decreases the maximum heat flow and creates a wider transient thermal anomaly. Transient effects, such as the interplay between the large-scale lithospheric thinning and depocenter-scale normal faulting and footwall exhumation creates a non-linear heat flow evolution during extension. Sedimentation of low conductivity sediments also alters the steady-state thermal field, by depressing the surface and basement heat flow and increasing the basement temperature values. Crustal thermal transient effects are attenuated within a few million years, while the overall asthenosphere anomaly decays within tens of million years.

Enhanced erosion and sedimentation facilitate ductile lower crustal deformation and elastic flexure of the weak lithosphere leading to

enhanced differential uplift of the basin margins and subsidence in the depocenters during the syn- and post-rift basin evolution. Our modelled unconformities and erosional truncations often observed at the basin margins and the overall basin stratigraphy are in a good agreement with observations in the Pannonian Basin system during its Miocene to Quaternary evolution.

Highest subsidence rates are recorded at different times in the different depocenters leading to diachronous transgressive-regressive cycles in different half-grabens overwriting any climatic signals. This also means that correlation of transgressive events within the Miocene half-grabens of the syn-rift basins is an incompatible exercise. Trapping basins and (dis)connections between the depocenters lead to rapid changes of the kilometre-scale palaeowater-depth differences during the syn-rift and early post-rift times.

Post-rift sedimentary evolution and facies distribution is controlled mainly by the high sediment supply and continuous fast subsidence. Enhanced eustatic and climatic variations facilitate autogenic processes leading to more frequent fluvio-deltaic avulsion events and creating pronounced unconformities. Furthermore, this lateral migration of the delta system on the shelf controls the along-strike variation of the sediment input and coeval transgression and regression overwriting eustatic forcing.

Structural restoration of the folded sediments and decompaction of the shelf margin slope clinoforms give a correct estimate of the paleo bathymetry of the basins at the time of slope progradation. Our simplified models give an estimate of 650 m water depth by the time of post-rift progradation in the Danube Basin, although the observed compacted height of these clinoforms is only 340 m. Our model also predicts that preceding water depth prior to the deposition of the deep water turbiditic secession could have reached more than 1000 m in this region.

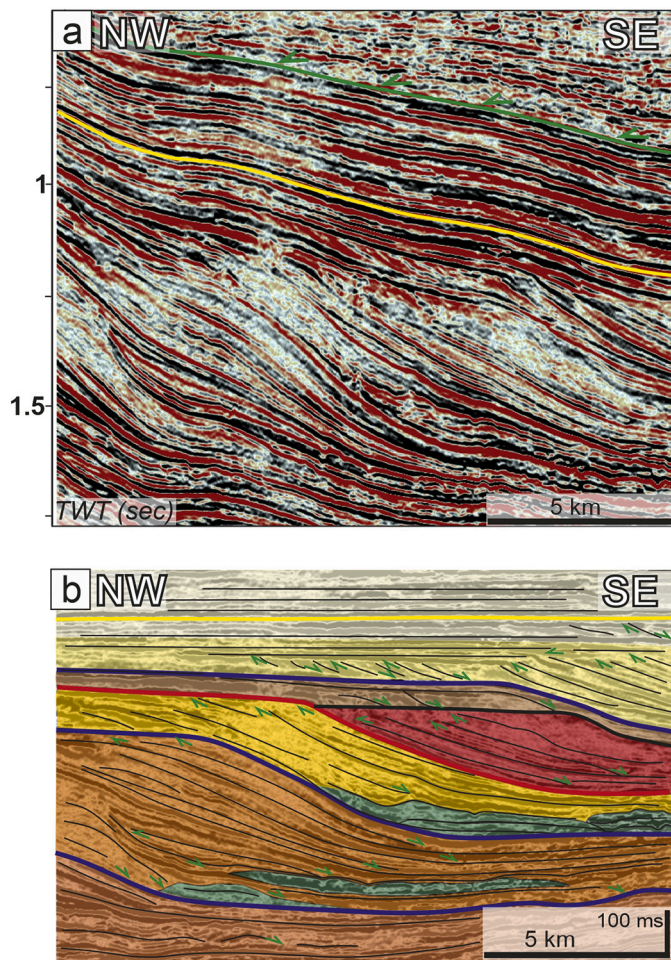


Fig. 13. a) Seismic section (modified after Balázs et al., 2018a) oriented parallel with the direction of post-rift shelf-margin slope progradation in the Jászág subbasin. For location see Fig. 1. The interpretation shows typical progradational (in orange), aggradational (in yellow), forced regression (in red), and retrogradational (in brown) patterns in the Great Hungarian Plain. Note the turbidite complexes at the toe of slopes (in green) and the small-scale prograding deltas on the shelf. Green half-arrows are reflection terminations. Green horizon is the unconformity between Miocene and Pliocene sediments, yellow horizon is the flattening level. b) Flattened version of the seismic lines above. (For interpretation of the references to colour in this figure legend, the reader is referred to the web version of this article.)

Declaration of Competing Interest

The authors declare that they have no known competing financial interests or personal relationships that could have appeared to influence the work reported in this paper.

Acknowledgements

We dedicate this study to the memory of Ferenc “Frank” Horváth, one of the pioneers of sedimentary basin analysis. AB acknowledges financial support from the ETH Zurich Postdoctoral Fellowship programme and academic support of the Hungarian Science Foundation (K 129279). Numerical modelling has been carried out at Utrecht University. Fruitful discussions with László Lenkey on the thermal evolution of the Pannonian Basin are acknowledged. We thank Piotr Krzywiec and an anonymous reviewer for their detailed and constructive reviews that significantly improved the quality of the manuscript. The commercial stratigraphic numerical code used in this study can be requested by contacting Beicip-Franlab (www.beicip.com). We thank Beicip-Franlab

for providing an academic license for DionisosFlow.

Appendices. Supplementary data

Supplementary data to this article can be found online at <https://doi.org/10.1016/j.gloplacha.2020.103386>.

References

- Andrés-Martínez, M., Pérez-Gussinyé, M., Armitage, J., Morgan, J.P., 2019. Thermomechanical implications of sediment transport for the architecture and evolution of continental rifts and margins. *Tectonics* 38, 641–665.
- Andrić, N., Sant, K., Matenco, L., Mandić, O., Tomljenović, B., Pavelić, D., Ooms, J., 2017. The link between tectonics and sedimentation in asymmetric extensional basins: Inferences from the study of the Sarajevo-Zenica Basin. *Mar. Pet. Geol.* 83, 305–322.
- Armitage, J.J., Duller, R.A., Whittaker, A.C., Allen, P.A., 2011. Transformation of tectonic and climatic signals from source to sedimentary archive. *Nat. Geosci.* 4, 231–235. <https://doi.org/10.1038/NGEO1087>.
- Bada, G., Horváth, F., Dövényi, P., Szafián, P., Windhoffer, G., Cloetingh, S., 2007. Present-day stress field and tectonic inversion in the Pannonian basin. *Glob. Planet. Chang.* 58, 165–180.
- Balázs, A., Burov, E., Matenco, L., Vogt, K., Francois, T., Cloetingh, S., 2017a. Symmetry during the syn- and post-rift evolution of extensional back-arc basins: the role of inherited orogenic structures. *Earth Planet. Sci. Lett.* 462, 86–98.
- Balázs, A., Granjeon, D., Matenco, L., Sztanó, O., Cloetingh, S., 2017b. Tectonic and climatic controls on asymmetric half-graben sedimentation: Inferences from 3-D numerical modeling. *Tectonics* 36, 2123–2141. <https://doi.org/10.1002/2017TC004647>.
- Balázs, A., Magyar, L., Matenco, L., Sztanó, O., Tóké, L., Horváth, F., 2018a. Morphology of a large paleolake: analysis of compaction in the Miocene-Quaternary Pannonian Basin. *Glob. Planet. Chang.* 171, 134–147. <https://doi.org/10.1016/j.gloplacha.2017.10.012>.
- Balázs, A., Matenco, L., Vogt, K., Cloetingh, S., Gerya, T., 2018b. Extensional polarity change in continental rifts: Inferences from 3-D numerical modeling and observations. *J. Geophys. Res. Solid Earth* 123, 8073–8094. <https://doi.org/10.1029/2018JB015643>.
- Balla, Z., 1987. Cenozoic paleomagnetic data for the Carpatho-Pannonian region in the light of Miocene rotation kinematics. *Tectonophysics* 139, 67–98.
- Ballato, P., Brune, S., Strecker, M.R., 2019. Sedimentary loading–unloading cycles and faulting in intermontane basins: Insights from numerical modeling and field observations in the NW Argentine Andes. *Earth Planet. Sci. Lett.* 506, 388–396.
- Ballmer, M.D., Ito, G., van Hunen, J., Tackley, P.J., 2010. Small-scale sublithospheric convection reconciles geochemistry and geochronology of ‘Superplume’ volcanism in the western and South Pacific. *Earth Planet. Sci. Lett.* 290, 224–232.
- Bialas, R., Buck, W.R., 2009. How sediment promotes narrow rifting: Application to the Gulf of California. *Tectonics* 28. <https://doi.org/10.1029/2008TC002394>. TC4014.
- Böhme, M., 2003. Miocene climatic optimum: evidence from lower vertebrates of Central Europe. *Palaeogeogr. Palaeoclimatol. Palaeoecol.* 195, 389–401.
- Buck, W.R., 1986. Small-scale convection induced by passive rifting: the cause for uplift of rift shoulders. *Earth Planet. Sci. Lett.* 77 (3–4), 362–372.
- Burgess, P.M., Masiero, I., Toby, S.C., Duller, R.A., 2019. A big fan of signals? Exploring autogenic and allogenic process and product in a numerical stratigraphic forward model of submarine-fan development. *J. Sediment. Res.* 89, 1–12. <https://doi.org/10.2110/jsr.2019.3>.
- Burov, E., Poliakov, A., 2003. Erosional forcing of basin dynamics: new aspects of syn- and post-rift evolution. *Geol. Soc. Spec. Pub. London* 212, 209–223.
- Burov, E., Yamato, P., 2008. Continental plate collision, P-T-t conditions and unstable vs. stable plate dynamics: Insights from thermo-mechanical modelling. *Lithos* 103, 178–204. <https://doi.org/10.1016/j.lithos.2007.09.014>.
- Childs, C., Manzocchi, T., Walsh, J.J., Bonson, C.G., Nicol, A., Schöpfer, M.P.J., 2009. A geometric model of fault zone and fault rock thickness variations. *J. Struct. Geol.* 31, 117–127. <https://doi.org/10.1016/j.jsg.2008.08.009>.
- Csató, I., Granjeon, D., Catuneanu, O., Baum, G.R., 2013. A three-dimensional stratigraphic model for the Messinian crisis in the Pannonian Basin, eastern Hungary. *Basin Res.* 25, 121–148. <https://doi.org/10.1111/j.1365-2117.2012.00553.x>.
- Csató, I., Catuneanu, O., Granjeon, D., 2014. Millennial-scale sequence stratigraphy: numerical simulation with Dionisos. *J. Sediment. Res.* 84, 394–406.
- Csontos, L., Vörös, A., 2004. Mesozoic plate tectonic reconstruction of the Carpathian region. *Palaeogeogr. Palaeoclimatol. Palaeoecol.* 210 (1), 1–56. <https://doi.org/10.1016/j.palaeo.2004.02.033>.
- Dias, A.E., Lavier, L.L., Hayman, N.W., 2015. Conjugate rifted margins width and asymmetry: the interplay between lithospheric strength and thermomechanical processes. *J. Geophys. Res. Solid Earth* 120, 8672–8700. <https://doi.org/10.1002/2015JB012074>.
- Dressel, I., Scheck-Wenderoth, M., Cacace, M., 2017. Backward modelling of the subsidence evolution of the Colorado Basin, offshore Argentina and its relation to the evolution of the conjugate Orange Basin, offshore SW Africa. *Tectonophysics* 716, 168–181.
- Dunkl, I., Frisch, W., 2002. Thermochronologic constraints on the Late Cenozoic exhumation along the Alpine and West Carpathian margins of the Pannonian basin. *EGU Stephan Mueller Special Publication Series* 3, 135–147.

- Duret, T., Petri, B., Mohn, G., Schmalholz, S.M., Schenker, F.L., Muntener, O., 2016. The importance of structural softening for the evolution and architecture of passive margins. *Sci. Rep.* 6 (1), 38704. <https://doi.org/10.1038/srep38704>.
- Ebner, F., Saschenhofer, R.F., 1995. Palaeogeography, subsidence and thermal history of the Neogene Styrian Basin (Pannonian basin system, Austria). *Tectonophysics* 242, 133–150. [https://doi.org/10.1016/0040-1951\(94\)00155-3](https://doi.org/10.1016/0040-1951(94)00155-3).
- Erdos, Z., Huismans, R.S., van der Beek, P., Thieulot, C., 2014. Extensional inheritance and surface processes as controlling factors of mountain belt structure. *J. Geophys. Res. Solid Earth* 119, 9042–9061.
- Faccenna, C., Becker, T.W., Auer, L., Billi, A., Boschi, L., Brun, J.P., Capitanio, F.A., Funicello, F., Horvath, F., Jolivet, L., 2014. Mantle dynamics in the Mediterranean. *Rev. Geophys.* 52, 283–332. <https://doi.org/10.1002/2013RG000444>.
- Fodor, L., Csontos, L., Bada, G., Györfi, I., Benkovics, L., 1999. Tertiary tectonic evolution of the Pannonian basin system and neighbouring orogens: a new synthesis of paleostress data. In: Durand, B., Jolivet, L., Horvath, F., Séranne, M. (Eds.), *The Mediterranean Basins: Tertiary Extension within the Alpine Orogen*. Blackwell Sciences Special Publications of the Geological Society of London, Oxford, pp. 295–334.
- Fodor, L., Bada, G., Csillag, G., Horvath, E., Ruszkiczay-Rudiger, Z., Palotas, K., Sikhegyi, F., Timar, G., Cloetingh, S., 2005. An outline of neotectonic structures and morphotectonics of the western and central Pannonian Basin. *Tectonophysics* 410, 15–41.
- Francois, T., Burov, E., Meyer, B., Agard, P., 2013. Surface topography as key constraint on thermo-rheological structure of stable cratons. *Tectonophysics* 602, 106–123. <https://doi.org/10.1016/j.tecto.2012.10.009>.
- Gervais, V., Masson, R., 2008. Numerical simulation of a stratigraphic model. *Comput. Geosci.* 12, 163–179. <https://doi.org/10.1007/s10596-008-9076-4>.
- Gong, C., Sztano, O., Steel, R.J., Xian, B., Galloway, W., Bada, G., 2019. Critical differences in sediment delivery and partitioning between marine and lacustrine basins: a comparison of marine and lacustrine aggradational to progradational clinothem pairs. *GSA Bull.* 131, 766–781.
- Granjeon, D., 2019. Use of high-performance stratigraphic forward modelling to improve siliciclastic and carbonate reservoir depositional architecture description. *Journal of the Japanese Association for Petroleum Technology* 84, 59–70.
- Granjeon, D., Joseph, P., 1999. Concepts and applications of a 3D multiple lithology, diffusive model in stratigraphic modelling. In: Harbaugh, J.W., Watney, W.L., Rankey, E.C., Slingerland, R., Goldstein, R.H., Franseen, E.K. (Eds.), *Numerical experiments in Stratigraphy, SEPM – Society of Sedimentary Geology*, 62. Special Publication, pp. 197–210. <https://doi.org/10.2110/pec.99.62.0197>.
- Harangi, Sz., Downes, H., Kósa, L., Szabó, Cs., Thirlwall, M.F., Mason, P.R.D., Matthey, D., 2001. Almandine Garnet in Calc-alkaline Volcanic Rocks of the Northern Pannonian Basin (Eastern–Central Europe): Geochemistry, Petrogenesis and Geodynamic Implications. *J. Petrol.* 42, 1813–1843. <https://doi.org/10.1093/ptology/42.10.1813>.
- Harris, A.D., Covault, J.A., Baumgardner, S., Sun, T., Granjeon, D., 2020. Numerical modeling of icehouse and greenhouse sea-level changes on a continental margin: Sea-level modulation of deltaic avulsion processes. *Mar. Pet. Geol.* 111, 807–814.
- Hart, N.R., Stockli, D.F., Lavier, L.L., Hayman, N.W., 2017. Thermal evolution of a hyperextended rift basin, Mauléon Basin, western Pyrenees: thermal evolution of hyperextended rift. *Tectonics*. <https://doi.org/10.1002/2016TC004365>.
- Henriksen, S., Helland-Hansen, W., Bullimore, S., 2011. Relationship between shelfedge trajectories and sediment dispersal along depositional dip and strike: a different approach to sequence stratigraphy. *Basin Res.* 23, 3–21.
- Heron, P.J., Pysklywec, R.N., Stephenson, R., 2016. Lasting mantle scars lead to perennial plate tectonics. *Nat. Commun.* 7, 11834 <https://doi.org/10.1038/ncomms11834>.
- Horvath, F., Royden, L., 1981. Mechanism for the formation of the intra-Carpathian basins: a review. *Earth Evol. Sci.* 3 (4), 307–316.
- Horvath, F., Musitz, B., Balázs, A., Végli, A., Uhrin, A., Nádor, A., Koroknai, B., Pap, N., Tóth, T., Wörum, G., 2015. Evolution of the Pannonian basin and its geothermal resources. *Geothermics* 53, 328–352.
- Hou, Y., Wang, H., Fan, T., Zhang, H., Yang, R., Li, Y., Long, S., 2020. Rift-related sedimentary evolution and its response to tectonics and climate changes: a case study of the Guaizihu sag, Yingen-Ejinaqi Basin, China. *J. Asian Earth Sci.*, 104370 <https://doi.org/10.1016/j.jseas.2020.104370>.
- Huismans, R.S., Beaumont, C., 2003. Symmetric and asymmetric lithospheric extension: relative effects of frictional-plastic and viscous strain softening. *J. Geophys. Res.* 108, 2496. <https://doi.org/10.1029/2002JB002026>.
- Hutchison, I., 1985. The effects of sedimentation and compaction on oceanic heat flow. *Geophys. J. Int.* 82, 439–459. <https://doi.org/10.1111/j.1365-246X.1985.tb05145.x>.
- Juhász, Gy., 1991. Lithostratigraphical and sedimentological framework of the Pannonian (s.l.) sedimentary sequence in the Hungarian Plain (Alföld), Eastern Hungary. *Acta Geol. Hung.* 34, 53–72.
- Kim, Y., Kim, W., Cheong, D., Muto, T., Pyles, D.R., 2013. Piping coarse-grained sediment to a deep water fan through a shelf-edge delta bypass channel: Tank experiments. *J. Geophys. Res. Earth Surf.* 118, 2279–2291. <https://doi.org/10.1002/2013JF002813>.
- Kováč, M., Andreyeva-Grigorovich, A., Bajraktarevic, Z., Brzobohatý, R., Filipescu, S., Fodor, L., Harzhauser, M., Nagymarosy, A., Oszczytko, N., Pavelic, D., 2007. Badenian evolution of the Central Paratethys Sea: paleogeography, climate and eustatic sea-level changes. *Geol. Carpath.* 58, 579–606.
- Kovács, Á., Balázs, A., Spelič, M., Sztano, O., 2021. Forced or normal regression signals in a lacustrine basin? Insights from 3D stratigraphic forward modelling in the SW Pannonian Basin. *Glob. Planet. Chang.* <https://doi.org/10.1016/j.gloplacha.2020.103376>. In press.
- Lankreier, A., Kovac, M., Cloetingh, S., Pitonak, P., Hloska, M., Biermann, C., 1995. Quantitative subsidence analysis and forward modelling of the Vienna and Danube basins; thin-skinned versus thick-skinned extension. *Tectonophysics* 252 (1–4).
- Le Pourhiet, L., Burov, E., Moretti, I., 2004. Rifting through a stack of inhomogeneous thrusts (the dipping pie concept). *Tectonics* 23, TC4005. <https://doi.org/10.1029/2003TC001584>.
- Lenkey, L., Raáb, D., Goetzl, G., Lapanje, A., Nádor, A., Rajver, D., Rotár-Szalkai, Á., Svasta, J., Zekiri, F., 2017. Lithospheric scale 3D thermal model of the Alpine–Pannonian transition zone. *Acta Geod. Geophys.* 52, 161–182. <https://doi.org/10.1007/s40328-017-0194-8>.
- Leroux, E., Rabineau, M., Aslanian, D., Granjeon, D., Droz, L., Gorini, C., 2014. Stratigraphic simulations of the shelf of the Gulf of Lions: testing subsidence rates and sea-level curves during the Pliocene and Quaternary. *Terra Nova* 26, 230–238.
- Lescoutre, R., Tugend, J., Brune, S., Masini, E., Manatschal, G., 2019. Thermal evolution of asymmetric hyperextended magma-poor rift systems: results from numerical modeling and Pyreneanfield observations. *Geochem. Geophys. Geosyst.* 20, 4567–4587. <https://doi.org/10.1029/2019GC008600>.
- Liptai, N., Hidas, K., Tommasi, A., Patkó, L., Kovács, I.J., Griffin, W.L., O'Reilly, S.Y., Pearson, N.J., Szabó, C., 2018. Lateral and vertical heterogeneity in the lithospheric mantle at the northern margin of the Pannonian Basin reconstructed from peridotite xenolith microstructures. *J. Geophys. Res. Solid Earth* 124, 6315–6336.
- Lister, G.S., Etheridge, M.A., Symonds, P.A., 1986. Detachment faulting and the evolution of passive continental margins. *Geology* 14, 246–250.
- Magyar, I., Radivojevic, D., Sztano, O., Synak, R., Ujszászi, K., Pócsik, M., 2013. Progradation of the paleo-Danube shelf margin across the Pannonian Basin during the late Miocene and early Pliocene. *Glob. Planet. Chang.* 103, 168–173.
- Martins-Neto, M.A., Catuneanu, O., 2010. Rift Sequence Stratigraphy. *Mar. Pet. Geol.* 27, 247–253.
- Matenco, L., Haq, B., 2020. Multi-scale depositional successions in tectonic settings. *Earth-Sci. Rev.* 200, 102991 <https://doi.org/10.1016/j.earscirev.2019.102991>.
- Matenco, L., Munteanu, I., ter Borgh, M., Stanica, A., Tilita, M., Lericolais, G., Dinu, C., Oaie, G., 2016. The interplay between tectonics, sediment dynamics and gateways evolution in the Danube system from the Pannonian Basin to the western Black Sea. *Sci. Total Environ.* 543, 807–827. <https://doi.org/10.1016/j.scitotenv.2015.10.081>.
- Milia, A., Iannace, P., Tesauro, M., Torrente, M.M., 2018. Marsili and Cefalu basins: the evolution of a rift system in the southern Tyrrhenian Sea (Central Mediterranean). *Glob. Planet. Chang.* 171, 225–237. <https://doi.org/10.1016/j.gloplacha.2017.12.003>.
- Nagymarosy, A., Hámor, G., 2012. Genesis and evolution of the Pannonian Basin. In: Haas, J. (Ed.), *Geology of Hungary, Regional Geology Reviews*. Springer, pp. 149–200.
- Naliboff, J.B., Buitter, S.J.H., Péron-Pinvidic, G., Osmundsen, P.T., Tetreault, Y., 2017. Complex fault interaction controls continental rifting. *Nat. Commun.* 8, 1179. <https://doi.org/10.1038/s41467-017-00904-x>.
- Olive, J., Behn, M., Malatesta, L., 2014. Modes of extensional faulting controlled by surface processes. *Geophys. Res. Lett.* 41, 6725–6733. <https://doi.org/10.1002/2014GL015107>.
- Pavelic, D., Kovacic, M., 2018. Sedimentology and stratigraphy of the Neogene rift-tube North Croatian Basin (Pannonian Basin System, Croatia): a review. *Mar. Pet. Geol.* 91, 455–469.
- Petersen, K., Schiffer, C., 2016. Wilson cycle passive margins: Control of orogenic inheritance on continental breakup. *Gondwana Res.* 39, 131–144. <https://doi.org/10.1016/j.jgr.2016.06.012>.
- Pigott, J., Radivojevic, D., 2010. Seismic stratigraphy based chronostratigraphy (SSBC) of the Serbian Banat region of the Pannonian Basin. *Center Eur. J. Geogr.* 2, 481–500. <https://doi.org/10.2478/v10085-010-0027-2>.
- Poliakov, A.N.B., Cundall, P., Podlachikov, Y., Laykivsky, V., 1993. An explicit inertial method for the simulation of viscoelastic flow: An evaluation of elastic effects on diapiric flow in two or three-layers models. In: Stone, D.B., Runcorn, S.K. (Eds.), *Flow and Creep in the Solar System: Observations, Modelling and Theory*, Dyn. Modell. Flow Earth Planet Series, pp. 175–195. https://doi.org/10.1007/978-94-015-8206-3_12.
- Porebski, S.J., Steel, R.J., 2003. Shelf-margin deltas: their stratigraphic significance and relation to Deepwater sands. *Earth Sci. Rev.* 62, 283–326.
- Postma, G., Kleverlaan, K., Cartigny, M.J.B., 2014. Recognition of cyclic steps in sandy and gravelly turbidite sequences, and consequences for the Bouma facies model. *Sedimentology* 61, 2268–2290.
- Ramsay, T., Pysklywec, R., 2011. Anomalous bathymetry, 3D edge-driven convection, and dynamic topography at the western Atlantic passive margin. *J. Geodyn.* 52, 45–56. <https://doi.org/10.1016/j.jog.2010.11.008>.
- Royden, L., Keen, C.E., 1980. Rifting process and thermal evolution of the continental margin of eastern Canada determined from subsidence curves. *Earth Planet. Sci. Lett.* 51, 343–361.
- Ruszkiczay-Rüdiger, Zs, Dunai, T.J., Bada, G., Fodor, L., Horvath, E., 2005. Middle to late Pleistocene uplift rate of the Hungarian Mountain Range at the Danube Bend (Pannonian Basin) using in situ produced ³He. *Tectonophysics* 410 (1–4), 173–187.
- Schlager, W., 1993. Accommodation and supply—a dual control on stratigraphic sequences. *Sediment. Geol.* 86, 111–136.
- Schmid, S.M., Bernoulli, D., Fugenschuh, B., Matenco, L., Schefer, S., Schuster, R., Tischler, M., Ustaszewski, K., 2008. The Alpine–Carpathian–Dinaridic orogenic system: correlation and evolution of tectonic units. *Swiss J. Geosci.* 101, 139–183.
- Sebe, K., Selmečzi, I., et al., 2019. Miocene syn-rift lacustrine sediments in the Mecsek Mts. (SW Hungary). *Swiss J. Geosci.* 112, 83–100.
- Šujan, M., Braucher, R., Rybár, S., Maglay, J., Nagy, A., Fordinál, K., Šarinová, K., Šýkora, M., Józsa, S., Kováč, M., Team, A.S.T.E.R., 2018. Revealing the late Pliocene to Middle Pleistocene alluvial archive in the confluence of the Western Carpathian

- and Eastern Alpine rivers: 26Al/10Be burial dating from the Danube Basin (Slovakia). *Sediment. Geol.* 377, 131–146.
- Sztanó, O., Szafián, P., Magyar, I., Horányi, A., Bada, G., Hughes, D.W., Hoyer, D.L., Wallis, R.J., 2013. Aggradation and progradation controlled clinothems and deep-water sand delivery model in the Neogene Lake Pannon, Makó Trough, Pannonian Basin, SE Hungary. *Glob. Planet. Chang.* 103, 149–167.
- Sztanó, O., Kováč, M., Magyar, I., Šujan, M., Fodor, L., Uhrin, A., Rybár, S., Csillag, G., Tóké, L., 2016. Late Miocene sedimentary record of the Danube/Kisalföld Basin: interregional correlation of depositional systems, stratigraphy and structural evolution. *Geol. Carpath.* 67, 525–542.
- Tari, G., Dovenyi, P., Dunkl, I., Horvath, F., Lenkey, L., Ștefănescu, M., Szafian, P., Toth, T., 1999. In: Durand, B., Jolivet, L., Horvath, F., Serrane, M. (Eds.), *Lithospheric structure of the Pannonian basin derived from seismic, gravity and geothermal data, in the Mediterranean Basins: Extension within the Alpine Orogen*. *Geol. Soc. London Spec. Publ.*, pp. 215–250, 156.
- Ter Voorde, M., Bertotti, G., 1994. Thermal effects of normal faulting during rifted basin formation. 1. A finite difference model. *Tectonophysics* 240, 133–144.
- Theissen, S., Rüpke, L.H., 2010. Feedbacks of sedimentation on crustal heat flow: New insights from the Vøring Basin, Norwegian Sea. *Basin Res.* 22, 976–990. <https://doi.org/10.1111/j.1365-2117.2009.00437.x>.
- Theunissen, T., Huismans, R., 2019. Long-term coupling and feedback between tectonics and surface processes during non-volcanic rifted margin formation. *J. Geophys. Res. Solid Earth* 124, 12323–12347. <https://doi.org/10.1029/2018JB017235>.
- Tucker, G.E., Hancock, G.R., 2010. Modelling landscape evolution. *Earth Surf. Process. Landf.* 35, 28–50.
- Tucker, G.E., Slingerland, R., 1994. Erosional dynamics, flexural isostasy and long-lived escarpments: a numerical modeling study. *J. Geophys. Res.* 10, 229–243.
- Ueda, K., Willett, S.D., Gerya, T., Ruh, J., 2015. Geomorphological–thermo-mechanical modeling: Application to orogenic wedge dynamics. *Tectonophysics* 659, 12–30.
- Uhrin, A., Sztanó, O., 2011. Water-level changes and their effect on Deepwater sand accumulation in a lacustrine system: a case study from the late Miocene of western Pannonian Basin, Hungary. *Int. J. Earth Sci.* 101, 1427–1440. <https://doi.org/10.1007/s00531-011-0741-4>.
- Ustaszewski, K., Kounov, A., Schmid, S.M., Schaltegger, U., Krenn, E., Frank, W., Fügenschuh, B., 2010. Evolution of the Adria-Europe plate boundary in the northern Dinarides: from continent-continent collision to back-arc extension. *Tectonics* 29. <https://doi.org/10.1029/2010tc002668>. TC6017.
- Whipple, K.X., 2009. The influence of climate on the tectonic evolution of mountain belts. *Nat. Geosci.* 2, 97–104. <https://doi.org/10.1038/ngeo413>.
- Wu, H., Ji, Y., Wu, C., Duclaux, G., Wu, H., Gao, C., Li, L., Chang, L., 2018. Stratigraphic response to spatiotemporally varying tectonic forcing in rifted continental basin: Insight from a coupled tectonic-stratigraphic numerical model. *Basin Res.* <https://doi.org/10.1111/bre.12322>.
- Yang, W., Kominz, M.A., Major, R.P., 1998. Distinguishing the roles of autogenic versus allogenic processes in cyclic sedimentation, Cisco Group (Virgilian and Wolfcampian), north-Central Texas. *GSA Bull.* 110, 1333–1353.